How Circular Dichroism in Time- and Angle-Resolved Photoemission Can Be Used to Spectroscopically Detect Transient Topological States in Graphene

Michael Schüler,[1] Umberto De Giovannini,[2,3] Hannes Hübener,[3] Angel Rubio,[2,3,4]
Michael A. Sentef,[3] Thomas P. Devereaux,[1,5] and Philipp Werner[6]

[1]*Stanford Institute for Materials and Energy Sciences (SIMES), SLAC National Accelerator Laboratory,*
Menlo Park, California 94025, USA
[2]*Nano-Bio Spectroscopy Group, Departamento de Fisica de Materiales,*
Universidad del País Vasco UPV/EHU- 20018 San Sebastián, Spain
[3]*Max Planck Institute for the Structure and Dynamics of Matter,*
Luruper Chaussee 149, 22761 Hamburg, Germany
[4]*Center for Computational Quantum Physics (CCQ), The Flatiron Institute,*
162 Fifth Avenue, New York, New York 10010, USA
[5]*Department of Materials Science and Engineering, Stanford University, Stanford, California 94305, USA*
[6]*Department of Physics, University of Fribourg, 1700 Fribourg, Switzerland*

Pumping graphene with circularly polarized light is the archetype of light-tailoring topological bands. Realizing the induced Floquet-Chern-insulator state and demonstrating clear experimental evidence for its topological nature has been a challenge, and it has become clear that scattering effects play a crucial role. We tackle this gap between theory and experiment by employing microscopic quantum kinetic calculations including realistic electron-electron and electron-phonon scattering. Our theory provides a direct link to the build up of the Floquet-Chern-insulator state in light-driven graphene and its detection in time- and angle-resolved photoemission spectroscopy (ARPES). This approach allows us to study the robustness of the Floquet features against dephasing and thermalization effects. We also discuss the ultrafast Hall response in the laser-heated state. Furthermore, the induced pseudospin texture and the associated Berry curvature give rise to momentum-dependent orbital magnetization, which is reflected in circular dichroism in ARPES (CD-ARPES). Combining our nonequilibrium calculations with an accurate one-step theory of photoemission allows us to establish a direct link between the build up of the topological state and the dichroic pump-probe photoemission signal. The characteristic features in CD-ARPES are shown to be stable against heating and dephasing effects. Thus, tracing circular dichroism in time-resolved photoemission provides new insights into transient topological properties.

Subject Areas: Condensed Matter Physics

I. INTRODUCTION

Topological properties play an important role in a wide range of phenomena in condensed matter systems. In periodic systems, the notion of quantum-geometric properties like the Berry curvature and their implications on the macroscopic scale has become a central concept. The most prominent examples are topological insulators (TIs) and superconductors [1,2] with their protected surface or edge states. Realizing topological insulators with integer quantum anomalous Hall effect (QAHE) has proven to be a challenge. In this regard, the remarkable progress in creating two-dimensional (2D) materials and heterostructures thereof has opened new perspectives [3–6]. In 2D materials, the topology typically arises due to the Kane-Mele mechanism [7,8]: A gap opens at Dirac cones due to spin-orbit coupling, giving rise to band inversion and thus a topologically nontrival state. Monolayer graphene is a paradigmatic example, and many attempts have been made to turn graphene into a TI [9–11].

The possibility of opening a gap *dynamically* by pumping graphene with circularly polarized light was first proposed in Ref. [12]. In a Floquet picture, the periodic electric field renormalizes the band structure by virtual photon-emission and -absorption processes. By tailoring the pump frequency and strength, a Chern-insulating phase can be induced (Floquet-Chern insulator) [13], which shows features of a QAHE [14–16]. The concept of topological states engineered by periodic driving fields has been extended to experiments on ultracold atoms

[17,18], coherent excitations of the lattice degrees of freedom [19], more general classes of 2D materials [20], and different topological states such as Dirac and Weyl semimetals [21].

To trace the pump-induced transient changes of the electronic structure, time- and angle-resolved photoelectron spectroscopy (TR-ARPES) has been established as a state-of-the-art tool, which is well suited to capture Floquet physics [22]. Still, observing light-induced topological phases in experiments is a challenge. So far, the distinct features of a Floquet state—the gap opening and Floquet sidebands (replicas of the band structure associated with the absorbtion or emission of photons)—have been reported only for Bi_2Se_3 [23,24], although related effects like the dynamical Stark effect [25] or photodressed effective band structures [26] have been observed for different systems. As an alternative technique for detecting the induced topological state, time-resolved transport experiments on graphene show a pump-induced Hall response [27]. However, in these experiments, a pump-induced population imbalance also plays a role [28,29], and disentangling such effects from those of the induced Berry curvature is a nontrivial task. Furthermore, from these studies it becomes evident that scattering effects are crucial in graphene. In particular, the associated heating and dephasing effects compete with the coherence required for a Floquet state [30,31], although it is not clear yet which scattering mechanism is most important.

We address this challenge in the present work by considering the pump-induced dynamics in graphene including both electron-electron (*e-e*) and electron-phonon (*e*-ph) scattering. While *e-e* scattering determines the initial stages of thermalization [32] and is thus essential for the theoretical description, *e*-ph coupling is typically responsible for the relaxation of excited states back to equilibrium on a timescale of several hundred femtoseconds to picoseconds [33–35]. In a pumped system far from equilibrium, ultrafast *e*-ph scattering furthermore plays an important role in the population dynamics [36–42]. We focus explicitly on the experimentally relevant regime of weak to moderate pump field strength and map out the stability of the Floquet physics. Our many-body treatment is combined with a full treatment of the photoemission process, thus providing a *predictive* link to TR-ARPES.

In addition to mapping out the momentum-dependent band structure, ARPES can provide insights into the quantum properties of the initial state by exploiting the light polarization. For instance, the electron chirality and the pseudospin properties can give rise to distinct circular dichroism in graphene [43,44] or TI surface states [45,46]. More generally, momentum-dependent circular dichroism allows us to trace *orbital* angular momentum, which is intimately linked to the Berry curvature [47,48]. The latter quantity was rigorously mapped out for paradigmatic 2D systems—including graphene—in Ref. [49]. Measuring

dichroism in TR-ARPES will provide unprecedented insights into pump-induced topological properties [50].

It is the main focus of the present work to clarify this connection. Based on our predictive theory for TR-ARPES, which is combined with an accurate one-step calculation of the photoemission matrix elements, we map out the *induced* circular dichroism in laser-driven monolayer graphene. A comprehensive analysis of the Floquet state and its stability against interaction effects reveals that both *e-e* and *e*-ph scattering play an important role. Despite the thus reduced coherence, the circular dichroism is found to be robust even in the presence of strong dissipation, where other signatures of a Floquet state—that is, opening of a gap and sidebands—are strongly suppressed. Hence, the circular dichroism is a hallmark manifestation of the induced Floquet topological state, which provides conclusive insights where other methods struggle.

II. SETUP, MODEL, AND METHODS

The dynamics in graphene is modeled by the Hamiltonian

$$\hat{H}(t) = \hat{H}_0(t) + \hat{H}_{e\text{-}e} + \hat{H}_{e\text{-ph}}, \qquad (1)$$

where $\hat{H}_0(t)$ describes the free electronic structure including the light-matter interaction. We consider the next-nearest-neighbor tight-binding (TB) model defined by

$$\hat{H}_0(t) = \sum_{\mathbf{k}} \sum_{j,j',\sigma} h_{jj'}(\mathbf{k} - \mathbf{A}_p(t))\hat{c}^{\dagger}_{\mathbf{k}j\sigma}\hat{c}_{\mathbf{k}j'\sigma}. \qquad (2)$$

Here, $h_{jj'}(\mathbf{k})$ is the TB Hamiltonian in the subspace of p_z orbitals, while the pump pulse [vector potential $\mathbf{A}_p(t)$] is incorporated via the Peierls substitution. Under the assumption of sufficiently localized p_z orbitals, the full nonlinear light-matter coupling is included. Details are presented in the Appendix A.

The second term in Eq. (1) describes the *e-e* interaction. Scattering effects are taken into account at the level of an optimized Hubbard model ($U = 1.6J$ in units of the hopping amplitude J), which has been shown to accurately capture the electronic structure close to equilibrium [51]. We also include *e*-ph scattering by the last term in the Hamiltonian (1), taking the full dispersion of the transverse and longitudinal acoustic and optical modes into account. The matrix elements for the *e*-ph coupling can be obtained from the TB model [52,53]. We focus on in-plane phonon modes modulating the hopping J, which is the dominant mechanism for freestanding graphene [54].

The dynamics of the interacting system is treated efficiently within the time-dependent nonequilibrium Green's functions (TD-NEGF) approach [55]. Because of the relatively weak correlation effects, the second-order treatment with respect to the *e-e* and *e*-ph interaction provides an accurate description. Furthermore, we employ

the generalized Kadanoff-Baym ansatz (GKBA) [56], which reduces the otherwise enormous computational demands significantly, while retaining a good accuracy, as demonstrated in recent benchmark calculations [57–59]. Spectral properties are improved by spectral corrections to the GKBA [60]. All details on the methods can be found in Appendix C.

A. Time-resolved photoemission

The TD-NEGF approach provides a direct link to TR-ARPES [39,61] by

$$I(\mathbf{k}, \varepsilon_f, \Delta t) = \mathrm{Im} \sum_{jj'} \int_0^\infty dt \int_0^t dt' s(t) s(t') M_j^*(\mathbf{k}, p_\perp)$$
$$\times G_{jj'}^<(\mathbf{k}; t, t') M_{j'}(\mathbf{k}, p_\perp) e^{-i\Phi(t,t')}, \qquad (3)$$

where $\Phi(t, t') = \int_{t'}^t d\bar{t}[\omega_{\mathrm{pr}} - \varepsilon_{\mathbf{p}}(\bar{t})]$. Equation (3) represents a time-dependent generalization of the one-step photoemission intensity [62]: The transient electronic structure of the initial states is captured by the lesser Green's function $G_{jj'}^<(\mathbf{k}; t, t')$ (obtained from the TD-NEGF framework), while the coupling to the final states is determined by the matrix elements $M_j(\mathbf{k}, p_\perp)$. We compute $M_j(\mathbf{k}, p_\perp)$ by combining the TB model with a one-step theory of photoemission. Benchmarks against state-of-the-art calculations based on the time-dependent density-functional theory [22,63,64] ensure the predictive power of our approach (see Appendix B). The photoelectron momentum $\mathbf{p} = (\mathbf{k}, p_\perp)$ determines the energy in the absence of the pump pulse by $\varepsilon_f = \mathbf{p}^2/2$, while $\varepsilon_{\mathbf{p}}(t) = [\mathbf{p} - \mathbf{A}_p(t)]^2/2$ during the pump; the time-dependent phase factor $\Phi(t, t')$ takes the streaking of the continuum (laser-assisted photoemission, LAPE [65]) into account. The probe pulse is characterized by the central frequency ω_{pr} and the pulse envelope $s(t)$. We denote the delay between the pump and probe pulse by Δt [see Fig. 1(a)].

The pump photon energy is taken as $\omega_p = 1.5$ eV, which realizes a Floquet-Chern insulator with Chern number $C = 1$ [14]. This topological phase is robust against a small detuning of the pump energy. The peak field strength is chosen between $E_0 = 1 \times 10^{-3}$ and $E_0 = 4 \times 10^{-3}$ atomic units (a.u.) ($E_0 \simeq 0.05$ V/Å to $E_0 \simeq 0.2$ V/Å) corresponding to $I_0 = 3.5 \times 10^{10}$ W cm^{-2} to $I_0 = 5.6 \times 10^{11}$ W cm^{-2} peak intensity. The largest field strength is slightly above that of experimentally achievable pulses, but reveals the physics particularly clearly. All findings are generic and present also for weaker fields. The pump pulse is assumed to be left-handed circularly polarized (LCP) [see Fig. 1(a)], while we choose the envelope to contain 20 optical cycles ($T_p = 55$ fs duration) unless stated otherwise. The probe pulse is assumed to have the envelope $s(t) = \sin^2[\pi(t - \Delta t)/T_{\mathrm{pr}}]$ with a pulse length of $T_{\mathrm{pr}} = 26$ fs. Its polarization is assumed to be either right-handed circularly polarized (RCP) or LCP.
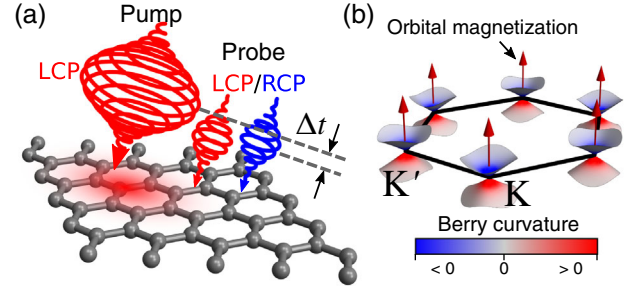

FIG. 1. (a) Sketch of a pump-probe TR-ARPES setup: A left-handed circularly polarized (LCP) pulse transiently dresses the electronic structure, which is probed by a right-handed circularly polarized (RCP), or LCP, short probe pulse. Delaying the probe pulse by Δt with respect to the pump provides access to real-time dynamics. (b) The induced Floquet-Chern insulator is characterized by nonzero Berry curvature in the lower effective band with the same sign at the two inequivalent Dirac points. The resulting net orbital magnetization gives rise to circular dichroism in photoemission spectroscopy.

We compute the corresponding TR-ARPES intensity $I_{\mathrm{LCP/RCP}}(\mathbf{k}, \varepsilon_f, \Delta t)$ according to Eq. (3), thus yielding the dichroic $I_{\mathrm{CD}}(\mathbf{k}, \varepsilon_f, \Delta t) = I_{\mathrm{LCP}}(\mathbf{k}, \varepsilon_f, \Delta t) - I_{\mathrm{RCP}}(\mathbf{k}, \varepsilon_f, \Delta t)$ and unpolarized signal $I_{\mathrm{tot}}(\mathbf{k}, \varepsilon_f, \Delta t) = I_{\mathrm{LCP}}(\mathbf{k}, \varepsilon_f, \Delta t) + I_{\mathrm{RCP}}(\mathbf{k}, \varepsilon_f, \Delta t)$. For the photon energy of the probe pulse we choose the value $\hbar\omega_{\mathrm{pr}} = 52$ eV, which is sufficient to detect photoelectrons from the Dirac points. Furthermore, scattering effects from the lattice have been found to be minimal at this energy, such that the intrinsic dichroism dominates [44].

The full time-dependent treatment based on the TR-ARPES expression (3) is complemented by a Floquet theory in the steady-state regime, where we assume that each lattice site is coupled to a thermalizing bath. This model provides a generic dissipation channel, which allows us to investigate dephasing and dissipation effects beyond e-e and e-ph scattering. Full details are presented in Appendix D.

B. Induced pseudospin texture and topological properties

To connect the photoemission theory to the light-induced topological properties, let us start by discussing the nature of the Floquet state. The energy spectrum is obtained from the Floquet Hamiltonian

$$[\hat{\mathcal{H}}_{nn'}]_{jj'}(\mathbf{k}) = \frac{1}{T_p} \int_0^{T_p} dt h_{jj'}(\mathbf{k} - \mathbf{A}_p(t)) e^{i(n-n')\omega_p t}$$
$$- n\omega_p \delta_{nn'}\delta_{jj'}, \qquad (4)$$

which captures all steady-state effects including photodressing and sidebands. A simple physical picture is obtained by applying Brillouin-Wigner theory [14], which yields the effective Hamiltonian $\hat{h}_{\mathrm{eff}}(\mathbf{k}) =$

$\sum_{n \neq 0} \hat{\mathcal{H}}_{0n}(\mathbf{k}) \hat{\mathcal{H}}_{n0}(\mathbf{k})/n\omega_p$ dressed by virtual absorption and emission processes. Within this picture, a circularly polarized pump field induces next-nearest-neighbor hoppings with a complex phase, thus opening a gap Δ at the two inequivalent Dirac points K, K'. The finite gap Δ corresponds to an occupation imbalance of the two equivalent sublattice sites $j = A, B$, resulting in a *finite* Berry curvature [66]. Depending on the frequency and field strength of the periodic drive, the effective Hamiltonian can be tailored to be a Chern insulator, with the Chern number determined by the specifics of the pump [14]. For a strong enough high-frequency pump, a nonequilibrium Hall response close to the quantized value can be realized within this model [14–16].

The emergence of the gap Δ is directly connected to the pseudospin properties with respect to the A, B sublattice sites. The effective Hamiltonian can be expressed as $\hat{h}_{\mathrm{eff}}(\mathbf{k}) = \mathbf{D}(\mathbf{k}) \cdot \hat{\boldsymbol{\sigma}}$ ($\hat{\boldsymbol{\sigma}}$ is the vector of Pauli matrices acting on the sublattice space); the vector $\mathbf{D}(\mathbf{k})$ characterizes the pseudospin structure of the Hamiltonian. Expanding around the Dirac points, one finds $\mathbf{D}(K + \mathbf{k}) \approx (-v_G k_y, v_G k_x, v_G^2 a_0 E_0^2/\omega_p^3)$ and $\mathbf{D}(K' + \mathbf{k}) \approx (v_G k_y, v_G k_x, -v_G^2 a_0 E_0^2/\omega_p^3)$ with $v_G = 3Ja_0/2$ (lattice constant a_0) [66]. The gap thus scales as

$$\Delta = D_z(K) \propto \frac{E_0^2}{\omega_p^3}. \tag{5}$$

Similarly, the quantum state of the lower (or upper) effective band is characterized by the orbital pseudospin vector $\mathbf{r}(\mathbf{k})$; in particular, $r_z(\mathbf{k}) = P_A(\mathbf{k}) - P_B(\mathbf{k})$ measures the occupation difference between the A and B sublattice at a specific point in momentum space. The pseudospin $r_z(\mathbf{k})$ is directly related to the topological properties. One can show that the bands are topologically trivial if $D_z(\mathbf{k})$ does not change sign across the BZ. In this case, one finds $r_z(\mathbf{k}) > 0$ [$r_z(\mathbf{k}) < 0$] for $D_z(\mathbf{k}) > 0$ [$D_z(\mathbf{k}) < 0$] in the whole BZ corresponding to a charge-density-wave pattern. In contrast, a topological phase transition is accompanied by $D_z(\mathbf{k})$ changing sign, resulting in a band inversion. Instead, for graphene in equilibrium and for the idealized limit of vanishing spin-orbit coupling $r_z(\mathbf{k}) = 0$, which implies vanishing Berry curvature.

Figure 2(b) shows the band structure of the effective Hamiltonian $\hat{h}_{\mathrm{eff}}(\mathbf{k})$ for $E_0 = 2 \times 10^{-3}$ and $E_0 = 4 \times 10^{-3}$ a.u. along with the pseudospin properties. The lower (upper) effective band with energy $\varepsilon_l(\mathbf{k})$ [$\varepsilon_u(\mathbf{k})$] is characterized by $r_z(\mathbf{k}) > 0$ [$r_z(\mathbf{k}) < 0$]. In Figs. 2(c) and 2(d), we show the Berry curvature $\Omega(\mathbf{k})$ of the lower band and the associated *orbital* polarization

$$m_z(\mathbf{k}) = -\frac{e}{\hbar}[\varepsilon_u(\mathbf{k}) - \varepsilon_l(\mathbf{k})]\Omega(\mathbf{k}) \tag{6}$$

from the modern theory of polarization [67,68]. As sketched in Fig. 1(b), this orbital magnetic moment possesses the

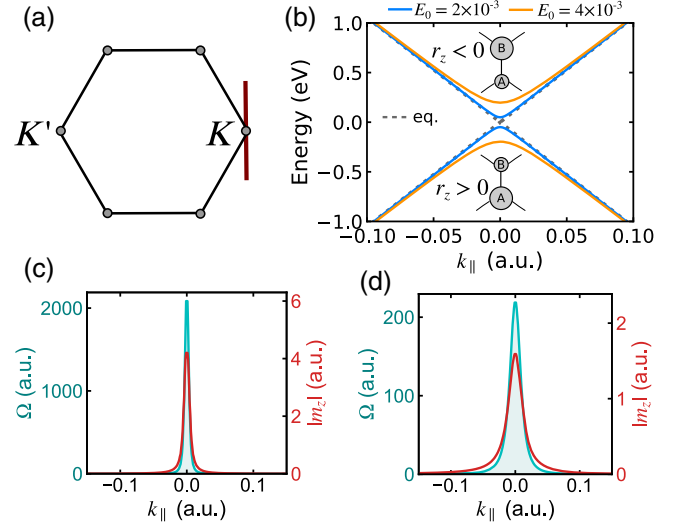
FIG. 2. (a) Path in the first Brillouin zone (BZ) close to the K point considered here. (b) Band structure of the effective Hamiltonian $\hat{h}_{\mathrm{eff}}(\mathbf{k})$ compared to the equilibrium bands along the path shown in (a). The insets illustrate the orbital pseudospin. (c),(d) Berry curvature $\Omega(\mathbf{k})$ and orbital polarization $m_z(\mathbf{k})$ of the effective lower band (calculated within second-order Brillouin-Wigner theory) for (c) $E_0 = 2 \times 10^{-3}$ and (d) $E_0 = 4 \times 10^{-3}$.

same symmetry properties as the Berry curvature; in particular, it has the same sign at K and K'. In the regime of weak pump driving strength considered here, the pseudospin and topological properties are fully characterized by their behavior in the vicinity of the Dirac points. Explicit calculation of the Chern number of the lower band of $\hat{h}_{\mathrm{eff}}(\mathbf{k})$ confirms $C = 1/2\pi \int d\mathbf{k} \Omega(\mathbf{k}) = 1$, with the dominant contribution coming from $\mathbf{k}$ close to K, K'. Hence, the topological character of the system is reflected directly by the orbital polarization (6) at the Dirac points. We remark that stronger fields can induce more complex pseudospin textures [69], while Floquet sidebands become important.

C. Orbital polarization and circular dichroism

In the absence of magnetic atoms, the induced orbital polarization (6) is an intrinsic topological property, which is due to the self-rotation of the underlying Bloch states. This relation can be understood intuitively by constructing wave packets $|W_{\mathbf{k}\alpha}\rangle$ from Bloch states in a particular band α. The finite spread in real space allows us to define the angular momentum $\langle \hat{L}_z \rangle_{\mathbf{k}\alpha} = \langle W_{\mathbf{k}\alpha}|\hat{L}_z|W_{\mathbf{k}\alpha}\rangle$. For a narrow distribution in momentum space, $\langle \hat{L}_z \rangle_{\mathbf{k}\alpha}$ becomes independent of the specific shape of the wave packet and thus defines the orbital angular momentum of the Bloch states itself [68], which is connected with the general orbital polarization $m_z(\mathbf{k}) = e/m \langle \hat{L}_z \rangle_{\mathbf{k}\alpha}$.

A nonzero orbital magnetic moment $m_z(\mathbf{k})$ determines the selection rules for photoexcitation properties [70] and thus results in *intrinsic* circular dichroism. In general,

circular dichroism arises from different contributions, such as scattering of the photoelectron from the lattice. This *extrinsic* effect is, for instance, responsible for the characteristic dichroic signal from graphene [71]. Averaging around high-symmetry points has been suggested as an efficient way of separating the contributions [49]. The wave-packet picture provides a direct link to intrinsic circular dichroism in photoemission [49] and reveals that the angular momentum $\langle \hat{L}_z \rangle_{\mathbf{k}\alpha}$ determines the selection rules; vanishing angular momentum corresponds to vanishing dichroism.

The magnetic moment $m_z(\mathbf{k})$ is intimately connected to the Berry curvature, as both quantities possess the same symmetry properties [48]. In particular, in the case of two (effective) bands, the orbital magnetic moment takes the form of Eq. (6) and thus becomes proportional to the Berry curvature. Hence, circular dichroism establishes a link to momentum-resolved topological properties. For two-orbital honeycomb lattice systems like graphene, this link can be found explicitly in terms of the orbital pseudospin texture. The leading contribution to the intrinsic dichroism in ARPES becomes [49]

$$I_{\mathrm{CD}}(\mathbf{k}, \varepsilon_f) \propto \frac{2}{k} r_z(\mathbf{k}) k_x a_{\mathrm{CC}} \tilde{\varphi}_z(k, p_\perp) \frac{d}{dk} \tilde{\varphi}_z(k, p_\perp)$$
$$\times \delta(\varepsilon_\alpha(\mathbf{k}) + \omega - \varepsilon_f). \quad (7)$$

Here, $\varepsilon_\alpha(\mathbf{k})$ is the energy of the valence band. The distance between the two carbon atoms is denoted by a_{CC}, while $\tilde{\varphi}_z(k, p_\perp)$ stands for the Fourier-transformed atomic p_z orbital. Hence, the dichroic signal is directly determined by the pseudospin properties. Within the quasistatic picture of periodically driven graphene outlined above, the induced pseudospin and topological properties are expected to manifest themselves in circular dichroism in TR-ARPES.

III. RESULTS

A. Floquet features and scattering processes

The simple physical picture based on the effective Brillouin-Wigner Hamiltonian provides a simple description of the opening of the effective bands but fails to take dynamical processes into account. To establish the link to TR-ARPES under experimentally relevant conditions, we now employ the full time-dependent treatment of the many-body Hamiltonian (2), with emphasis on the stability of the Floquet physics under e-e and e-ph scattering. Both mechanisms give rise to population redistribution, dephasing and, in the presence of e-ph coupling, dissipation.

1. Redistribution and heating

The dynamics of photoexcitation processes—especially far from equilibrium—is strongly influenced by scattering processes. Turning the e-e and e-ph interactions off, vertical transitions induced by the pump pulse lead to isolated points of nonzero population in the upper band determined by

energy and momentum conservation [Fig. 3(a), left panel]. The absorption of energy is limited by these restrictions; resonant driving will induce Rabi oscillations and even decrease the number of excited electrons. The picture changes dramatically when e-e scattering is included [Fig. 3(a), middle panel], since this leads to a thermalization of electrons (holes) in the upper (lower) band. The balance between the pumping strength and the scattering rate governs the effective Floquet thermalization [72,73]. In the limit of an infinitely long pulse, the system reaches a quasithermal distribution with infinite temperature. Similarly, e-ph scattering [Fig. 3(a), right panel] leads to a redistribution of the excited electrons, thus providing a pathway for further absorption. In contrast to e-e scattering, the dissipative character of e-ph scattering (if the phonons are considered as a heat bath with quasi-infinite heat capacity) gives rise to a Floquet steady state [73].

For a quantitative picture, we compute the time-dependent Green's function as described in Sec. II. To exclude that matrix-element effects mask the dynamics discussed here, we simplify the TR-ARPES formula (3) to

$$I(\mathbf{k}, \varepsilon_f, \Delta t) = \mathrm{Im} \sum_j \int_0^\infty dt \int_0^t dt' s(t) s(t') G_{jj}^<(\mathbf{k}; t, t')$$
$$\times e^{-i(\omega_{\mathrm{pr}} - \varepsilon_f)(t-t')} \quad (8)$$
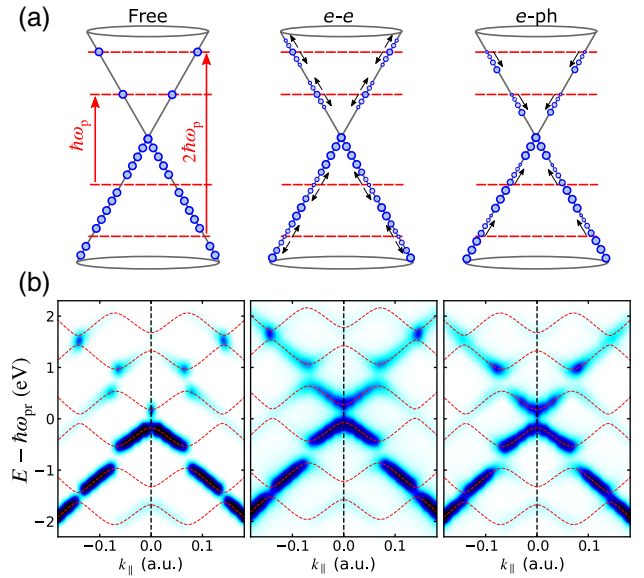

FIG. 3. (a) Illustration of the interplay between photoexcitation and scattering processes close to a Dirac point. (b) TR-ARPES spectra calculated with the simplified formula (8) with aligned pump ($E_0 = 4 \times 10^{-3}$ a.u.) and probe pulse, for the free system (left), including only e-e (middle) and only e-ph scattering (right panel), respectively. The spectra are calculated along the path shown in Fig. 2(a). The energy $E = \varepsilon_f - \mu$ is the kinetic energy of the photoelectrons shifted by the chemical potential $\mu = -4.6$ eV. The red dashed lines represent the band structure of the Floquet Hamiltonian (4).

for this discussion. We assume overlapping pump and probe pulses ($\Delta t = 0$) and express the energy in terms of the binding energy ε_b. The resulting spectra are presented in Fig. 3(b). The physical picture of scattering processes above is directly applicable to the TR-ARPES spectra. Without any interaction, only electrons at certain momenta are promoted to the excited-state manifold. The band structure captured by Eq. (8) now exhibits Floquet sideband features described by the Floquet Hamiltonian (4). The corresponding band structure is shown by the red dashed lines in Fig. 3. As Fig. 3(b) shows, the excited-state population is restricted to the avoided crossings of the Floquet bands.

Another important feature of the noninteracting treatment is the peak occupation directly at K just above $\varepsilon_b = 0$. This is a manifestation of a "topological hole" in quantum quenches [74]: Driving a topological phase transition and opening the gap, the orbital character is preserved. This effect is confined to the region close to K, where the time evolution is nonadiabatic no matter how slowly the pump pulse is switched on.

In contrast, the simulation with e-e scattering [Fig. 3(b), middle panel] yields a considerable redistribution of the occupation. In particular, the population close to K in the effective upper band becomes very pronounced, which is in stark contrast to the noninteracting case. Similar effects are observed as a result of e-ph scattering [Fig. 3(b), right panel], albeit high-energy features like the peak of the occupation at $\varepsilon_b = 1.5$ eV are suppressed due to the dissipation. We also note that the spectra of the interacting system align very well with the Floquet bands of the noninteracting system, which indicates that renormalization effects play a minor role (apart from a small energy shift in the presence of e-e interactions).

As also inferred from Fig. 3(b), the number of excited electrons is significantly larger if scattering channels are available, giving rise to considerably larger energy absorption. This behavior becomes clear when inspecting the

change of kinetic energy per particle ΔE [Fig. 4(a)]. While the pump pulse injects energy into the free system, this energy is mostly emitted back when the pump envelope approaches zero. This is in stark contrast to the result which includes e-e scattering, which leads to continuous heating and an order of magnitude larger absorption. e-ph scattering has a similar effect, even though the lack of full thermalization and cooling by emitting phonons reduces the kinetic energy. In contrast to e-e scattering, the effect of e-ph coupling depends on the effective band structure. Since the phonon spectrum is restricted to $\simeq 200$ meV, phonon-mediated relaxation across a gap $\Delta > 200$ meV becomes strongly suppressed due to a phonon "bottleneck" [39]. This effect is fully captured by our TD-NEGF approach (see Appendix C 2 for details).

2. Decoherence

The pronounced heating and the resulting dephasing effects—especially for resonant pumping as in graphene—typically hamper the coherence required for Floquet features [30,31]. Figure 4(b) shows representative photoemission spectra calculated from Eq. (8). Note that the broadening of the spectra is mostly due to decoherence effects, as the energy spectrum of the probe pulse is much narrower.

To investigate how the scattering effects influence the opening of a gap at K (or K'), we analyze $I(\mathbf{k} = K, \varepsilon_b, \Delta t = 0)$ by a two-peak Gaussian fit to extract the Floquet gap Δ presented in Fig. 4(b). Comparing to the gap Δ predicted by the noninteracting Brillouin Wigner theory (see Sec. II B), we find that e-e scattering reduces Δ only very weakly. As in Ref. [30], e-e interactions renormalize the band structure in the vicinity of the Dirac points, which increases Δ. However, this effect is compensated by the decoherence due to e-e scattering. In contrast, e-ph scattering has a strong effect, suppressing the Floquet gap almost completely for $E_0 \leq 2 \times 10^{-3}$. Consistent with Ref. [30], increasing the pump field strength stabilizes Δ.
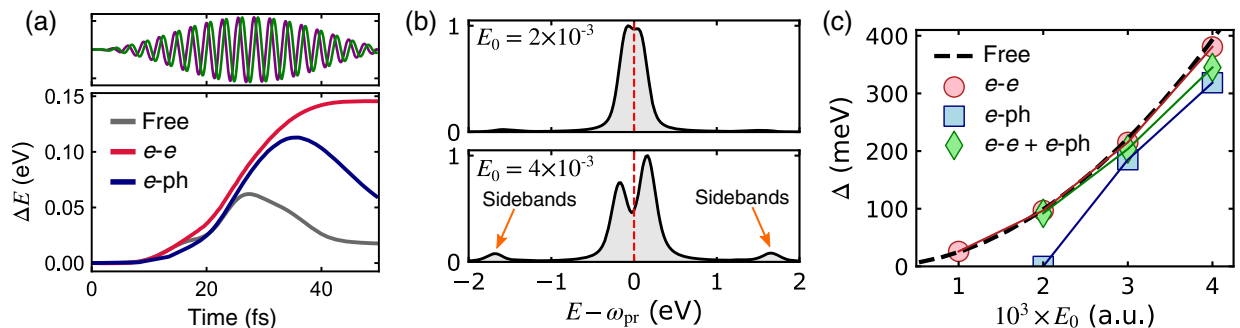

FIG. 4. (a) Time-dependent kinetic energy and shape of the pump pulse. The components of the circular pump fields are reported in purple (x) and green (y). (b) Photoemission spectra $I(\mathbf{k} = K, \varepsilon_f, \Delta t)$ [cf. Eq. (8)] at the Dirac point, including e-e and e-ph interactions. We use a pump pulse with $N_c = 30$ optical cycles. (c) Floquet gap Δ as a function of the pump field strength extracted from the spectra in (b) and Fig. 3(b). For the case of e-ph scattering, the broad spectra do not allow for an unambiguous determination of a gap.

To trace the origin of this pronounced effect, we switch off large-momentum e-ph scattering. The resulting spectra are considerably sharper, and the Floquet gap is much more pronounced. This shows that intervalley scattering is the predominant source of decoherence. Furthermore, for $E_0 \leq 3 \times 10^{-3}$ the Floquet gap is well within the phonon energy spectrum, while for larger E_0 the gap becomes larger than the maximum phonon energy. Thus, e-ph relaxation across the gap is suppressed, stabilizing Δ.

Including both e-e and e-ph scattering, this stabilization allows us to determine Δ for $E_0 \geq 2 \times 10^{-3}$. The Floquet gap is slightly larger than for e-ph coupling only. These results show that phonons are the major source of decoherence in this regime, while e-e scattering predominantly thermalizes the system.

Similar to the gap Δ, the Floquet sidebands remain stable in the presence of scattering effects, but they are broadened [see Fig. 4(b)]. The stability of the Floquet features (at least for stronger driving) is consistent with the ultrafast timescale of the pump pulse. The period of a single cycle is 2.7 fs, which is much shorter than any typical scattering time. Decoherence builds up over several pump cycles.

Scattering processes and the resulting heating and decoherence effects also strongly impact transport properties like the Hall response. In particular, decoherence was identified as a key factor [31] to understand ultrafast transport experiments [27], albeit on an empirical level. Investigating ultrafast scattering processes as captured by our theory thus provides a microscopic perspective on transport properties.

B. Ultrafast Hall response

The light-induced topological state in the considered regime is described by the effective Floquet Hamiltonian $\hat{h}_{\text{eff}}(\mathbf{k})$ (see Sec. II B), which yields a Chern number of $C = 1$ for the lower effective band. In the quasistatic picture, the system should thus exhibit a quantized Hall response in the limit of low effective temperatures [14]. However, the nonequilibrium situation in a pump-probe setup renders a straightforward detection and interpretation of the time-dependent Hall current difficult. Decoherence due to scattering processes will reduce the Floquet gap (see Sec. III A) and suppress the Hall response [28,29]. Increasing the pump strength stabilizes the Floquet features at the cost of stronger pump-induced heating.

The anomalous Hall response under pumping and including e-e and e-ph scattering can, in principle, be obtained from the GKBA time propagation. However, state-of-the-art experimental techniques enable the detection of ultrafast transient currents on the picosecond timescale, which is still a relatively long timescale for microscopic many-body simulations, so that a direct comparison is difficult.

1. Steady-state model

As we explain in Sec. III A, the e-e and e-ph interactions primarily lead to a redistribution of the occupation, while the effective band structure is governed by the free Floquet Hamiltonian. Moreover, the distribution is quasithermal with respect to the Floquet bands. In this situation, the Floquet nonequilibrium steady-state (NESS) formalism [75] provides an excellent description. Details are presented in Appendix D. In essence, we assume that each lattice site of graphene is coupled to a thermalizing bath (coupling strength γ), which is characterized by an effective temperature T_{eff}. This setup corresponds to a metallic substrate; however, here we treat it as a generic pathway for dissipation and dephasing.

The balance between absorption and dissipation determines the occupation of the Floquet bands. The NESS formalism yields the Green's function $G_{jj'}^{<}(\mathbf{k}, t, t')$ (which is now periodic in both time arguments). Inserting this expression into Eq. (8), and assuming an infinitely long pump and probe pulse yields

$$I(\mathbf{k}, \varepsilon_f) \propto \text{Im} \sum_j G_{jj}^{<}(\omega_{\text{pr}} - \varepsilon_f), \qquad (9)$$

where

$$G_{jj'}^{<}(\omega) = \frac{1}{T_p} \int_0^{T_p} dt_{\text{av}} \int_{-\infty}^{\infty} dt_{\text{rel}} e^{i\omega t_{\text{rel}}} \\ \times G_{jj'}^{<}\left(t_{\text{av}} + \frac{t_{\text{rel}}}{2}, t_{\text{av}} - \frac{t_{\text{rel}}}{2}\right). \qquad (10)$$

The NESS spectra obtained from Eq. (9) can be considered a very good fitting model for the TR-ARPES spectra; a quantitative comparison is shown in Sec. III D. Following Ref. [14], the Hall response can be directly obtained from the NESS model (see Appendix D for details). Fixing γ to match the line width of the TR-ARPES spectra in Fig. 4(b), the effective temperature T_{eff} remains the only free parameter.

2. Thermalization and effective temperature

To connect to the time-dependent microscopic treatment (including thermalization due to the scattering) and access the picosecond timescale, we employ a single-temperature model for the electronic temperature $T_{\text{el}}(t)$ adopted from Ref. [35]:

$$\frac{d}{dt} T_{\text{el}}(t) = \frac{\mathcal{I}(t)}{\alpha c_{\text{el}}(T_{\text{el}}(t))}, \qquad (11)$$

where $c_{\text{el}}(T)$ denotes the electronic heat capacity at temperature T, while $\mathcal{I}(t)$ represents the envelope of the intensity of the pump pulse. The parameter α is adjustable. Note that we ignore the phonon contribution here, as the
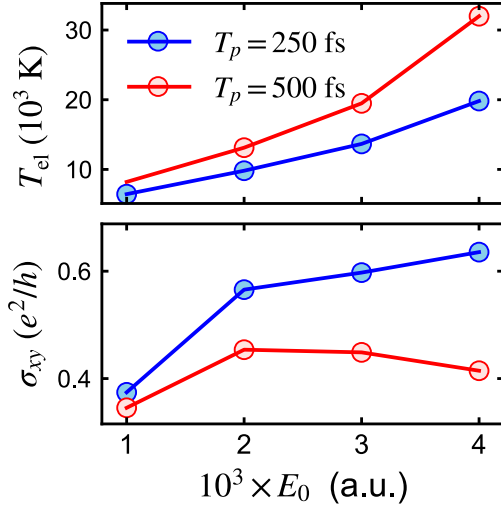
FIG. 5.   Upper panel: electronic temperature T_{el} obtained from the single-temperature model (11) for pump-pulse duration $T_p = 250$ fs (blue) and $T_p = 500$ fs (red) as a function of the pump field strength E_0. Lower panel: corresponding Hall response.

rapid thermalization of the phonon subsystem prevents cooling of electrons during the pump pulse. The model obtained by solving Eq. (11) is then fitted to the electronic temperature obtained from the GKBA simulation for varying length of the pump pulse.

With this model at hand, we can extrapolate $T_{el}(t)$ to longer timescales. Figure 5 shows the electronic temperature for a pulse duration of $T_p = 250$ fs and $T_p = 500$ fs. The system heats up considerably; one finds a scaling $T_{el} \sim E_0^2$ and roughly $T_{el} \sim T_p$ in the considered regime. The Hall response σ_{xy} (defined as the time average of the Hall current) is shown in the lower panel in Fig. 5. For $T_p = 250$ fs, σ_{xy} increases monotonically with E_0, although a saturation sets in for $E_0 \leq 2 \times 10^{-3}$. The maximum value reached is $\sigma_{xy} \approx 0.63 e^2/h$, which corresponds to approximately 32% of the quantized value $\sigma_{xy}^{(0)} = 2e^2/h$. Increasing the pump duration to $T_p = 500$ fs, the heating effects dominate for larger E_0, thus suppressing the Hall response with growing E_0. The quantized value $\sigma_{xy}^{(0)}$ cannot be approached in this regime.

In general, the nonequilibrium Hall response contains a topological contribution due to the induced Berry curvature (see Sec. II B) and a contribution arising from a probe-induced population imbalance [28]. The latter effect has been found to dominate for weak pump field strengths, as we use here [28]. Note that the NESS formalism employed here includes both contributions at the level of linear response. Isolating the Berry curvature contribution is a considerable task; this is where circular dichroism and the energy resolution of TR-ARPES can provide valuable complementary insights.

C. Time-resolved photoemission and circular dichroism

Now we investigate how the induced Berry curvature and pseudospin texture manifest themselves in the circular dichroism. To this end, we employ the full TR-ARPES expression (3) including photoemission matrix elements and laser dressing of the final states. The time-dependent Green's function entering Eq. (3) is computed taking both e-e scattering and e-ph scattering into account.

Figures 6(a) and 6(b) show the build up of the photo-dressed band structure captured by the unpolarized intensity $I_{tot}(\mathbf{k}, E, \Delta t)$ (the energy E is the kinetic energy of the photoelectron shifted by the chemical potential μ), and the corresponding dichroic signal $I_{CD}(\mathbf{k}, E, \Delta t)$. In the initial phase of the pump-induced dynamics ($\Delta t < 0$), Floquet features like a gap opening or sidebands are hardly visible, although a kink at $E - \omega_{pr} = -0.75$ eV indicates the onset of transient photodressing [Fig. 6(a)]. The portion of the pump pulse overlapping the probe pulse [see inset in Fig. 6(a)] is broad in frequency space; therefore, electrons are excited nonresonantly and redistributed by e-e and e-ph scattering. The dichroic signal resembles the equilibrium case [43,44] but with positive dichroism ($[I_{CD}(\mathbf{k}, E, \Delta t) > 0]$ for $E - \omega_{pr} < 0$. For aligned pump and probe pulses [Fig. 6(b)], the unpolarized spectrum combines features of the cases of e-e and e-ph scattering in Fig. 3(b). By switching off the corresponding phase factor in Eq. (3), we find that LAPE effects have little influence, apart from a slight enhancement of the sideband intensity relative to the zero-photon effective band. Inspecting $I_{CD}(\mathbf{k}, E, \Delta t = 0)$, a clear asymmetry becomes apparent. In particular, below $E - \omega_{pr} = 0$ close to the K point, positive dichroism (i.e., photoemission by a LCP probe pulse) dominates.

To investigate the dichroism in more detail, we integrate the TR-ARPES signal over a small region in momentum space in the vicinity of K,

$$N_{tot/CD}(E - \omega_{pr}) = \int d\mathbf{k} I_{tot/CD}(\mathbf{k}, \varepsilon_f, \Delta t = 0), \quad (12)$$

presented in Figs. 6(c) and 6(d) for $E_0 = 2 \times 10^{-3}$ and $E_0 = 4 \times 10^{-3}$. Close to $E - \omega_{pr} = 0$, the dichroism is pronounced and positive (negative) below (above) the Fermi energy. This sign change corresponds directly to the behavior of the pseudospin in Fig. 2(b). It is remarkable that our full one-step theory, which includes scattering of the photoelectron from the lattice, is in line with the simple physical picture outlined in Sec. II B. While intricate final-state effects have a profound impact on the concrete angular distribution of the dichroism, quantities integrated around high-symmetry points are more sensitive to *intrinsic* circular dichroism related to topological properties. We confirm this picture for several systems in Ref. [49]. Therefore, the dichroism observed in Figs. 6(c) and 6(d)
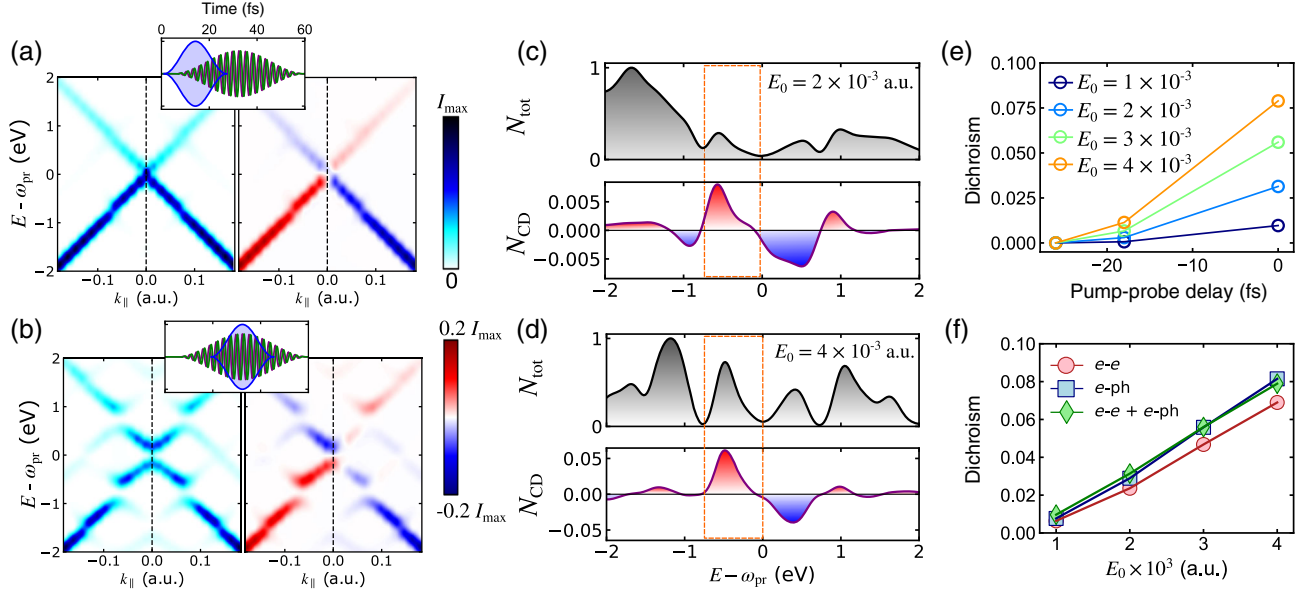
FIG. 6. (a),(b) Build up of Floquet features and circular dichroism in TR-ARPES for $\Delta t = -18$ fs (a) and $\Delta t = 0$ (b) calculated along the path depicted in Fig. 2(a). All spectra are obtained including e-e and e-ph scattering. The energy $E = \varepsilon_f - \mu$ is measured with respect to the chemical potential μ. The unpolarized intensity is shown in the left panels, while the dichroic spectra are shown on the right-hand side. (c),(d) Momentum-integrated unpolarized and dichroic TR-ARPES spectra (over a disk around K with $k_r = 0.25$ a.u. radius) for $E_0 = 2 \times 10^{-3}$ (c) and $E_0 = 4 \times 10^{-3}$ (d). The orange boxes indicate the range of energy integration for (e) and (f). (e) Relative integrated dichroic signal as a function of the pump-probe delay. (f) Dichroic signal as a function of the pump field strength.

arises due to the orbital magnetization and follows the proportionality to the pseudospin (7).

To quantify the circular dichroism relative to the unpolarized signal, we integrate $P_{\text{tot/CD}} = \int d\varepsilon N_{\text{tot/CD}}(\varepsilon)$ over the range indicated by the orange box in Figs. 6(c) and 6(d). The ratio $P_{\text{CD}}/P_{\text{tot}}$ is shown in Fig. 6(e) as a function of the pump-probe delay, which confirms that the build up of the dichroism follows the pump envelope. Inspecting $P_{\text{CD}}/P_{\text{tot}}$ for $\Delta t = 0$ [Fig. 6(f)], we find a roughly linear dependence on the pump field E_0. Although the pseudospin behaves as $r_z(\mathrm{K}) \propto E_0^2$ (which can be seen from Brillouin-Wigner theory), the heating effects, which increase with E_0, result in an overall linear behavior. As the system absorbs more energy if only e-e scattering is present, the dichroism is slightly reduced compared to the system with only e-ph scattering. Apart from such subtle effects, the dichroism is remarkably stable against dephasing and scattering. Note that the dichroism is sizable for $E_0 = 2 \times 10^{-3}$, where almost no Floquet gap can be observed [see Fig. 4(b)].

D. Robustness of the circular dichroism

The stability of the circular dichroism against interaction effects—in contrast to the Floquet gap—is a striking feature. To corroborate that this conclusion is not limited to the simplified model of e-e correlations, or an artifact of the specific treatment in this work, we perform calculations within the NESS formalism (see Appendix D for details).

Inserting the Green's function obtained from Eq. (10) into Eq. (3) and assuming an infinitely long pump and probe pulse yields

$$I(\mathbf{k}, \varepsilon_f) \propto \mathrm{Im} \sum_{jj'} M_j^*(\mathbf{k}, p_\perp) G_{jj'}^<(\omega_{\text{pr}} - \varepsilon_f) M_{j'}(\mathbf{k}, p_\perp).$$

$$(13)$$

Note that we neglect LAPE effects here. The Green's function is fully determined by the properties of the bath characterized by the coupling strength γ and the effective temperature T_{eff}.

Figure 7(a) illustrates that the Floquet NESS description of ARPES (13) provides a very good approximation of the full TR-ARPES treatment (3) for appropriate parameters γ and T_{eff}. Even though the agreement for the momentum-integrated signal N_{tot} is good, deviations indicate that the system exhibits a nonthermal distribution for overlapping pump and probe pulses [76]. The dichroic signal N_{CD}, however, agrees very well. On this basis, we can now increase the bath coupling strength γ, which also sets the dephasing timescale, and investigate the robustness of the circular dichroism. Performing an analysis as for Fig. 6(f), we calculate the relative energy-integrated dichroic signal for increasing γ. The result is presented in Fig. 7(b). The dichroism stays robust over a large range of dissipation strengths; more than doubling γ compared to the realistic
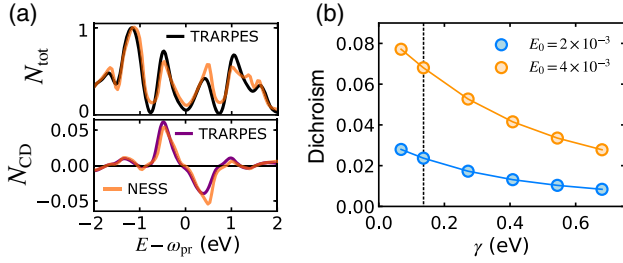
FIG. 7. (a) Comparison between the momentum-integrated unpolarized (upper) and dichroic (lower panel) signal for $E_0 = 4 \times 10^{-3}$ a.u. obtained from TR-ARPES [same as in Fig. 6(d)] and from the NESS formalism. The effective temperature is set to $T_{\text{eff}} = 1/30$ a.u. (b) Energy-integrated dichroism [extracted as in Fig. 6(f)] as a function of the bath coupling strength γ. The dashed vertical line indicates the value of γ in (a).

value used in Fig. 7(a) roughly reduces the dichroism by a factor of 2. We remark that γ also sets the linewidth of the photoemission spectra and thus captures the decoherence effects that we discuss in Sec. III A.

We also calculate photoemission spectra according to Eq. (13) for the values of γ from Fig. 7(b). The Floquet gap gets strongly suppressed for increasing dephasing γ, consistent with Ref. [29], up to a point where no gap can be observed anymore. Nevertheless, as Fig. 7(b) demonstrates, the circular dichroism stays robust even in this strongly dissipative regime.

IV. SUMMARY AND DISCUSSION

We presented a detailed investigation of the topological properties of graphene pumped with circularly polarized light under realistic conditions. Within the simple picture based on an effective renormalized Hamiltonian, a gap opens at the Dirac points, thus giving rise to nonzero Berry curvature and orbital polarization. In the considered regime of $\hbar\omega_p = 1.5$ eV pump photon energy and for realistic field strength, graphene becomes a Floquet-Chern insulator. While predicted within a noninteracting theory, we show that this induced topological state is robust against *e-e* and *e-*ph interactions for strong enough—but realistic—field strength of the pump laser.

Finding definite manifestations of the induced topological state in experiments is a challenge. The opening of a gap—as first reported in TR-ARPES experiments on Bi_2Se_3 [23,24]—would be a clear signature of the effective Floquet bands. Based on our time-dependent atomistic calculations including *e-e* and *e-*ph interactions, we show that the Floquet bands are formed but broadened by the dephasing due to the interactions. Both *e-e* and *e-*ph scattering are essential to capture the pronounced occupation of the excited bands. Heating effects would be severely underestimated by simulations which lack these scattering channels. The Floquet gap is found to be relatively stable

against interaction effects for larger pump field strengths, although *e-*ph coupling—predominantly intervalley scattering—gives rise to significant dephasing. For weak to moderate field strengths ($E_0 \leq 2 \times 10^{-3}$ a.u.), the Floquet gap is hardly visible, which implies that the opening of a gap is not a useful criterion for experiments in the considered regime.

In addition to the Floquet gap, the anomalous Hall current measured during the pump pulse—similar to the experiment in Ref. [27]—can provide insights into the induced topological state. Extrapolating to feasible time-scales by an effective temperature model, we find very pronounced heating effects (the effective electronic temperature can reach several 10 000 K). These heating effects (which increase with the field strength) compete with the stabilization of the Floquet gap, thus suppressing the Hall response far below the *quantized* value for realistically long pump pulses. In particular, for a pulse duration of $T_p = 500$ fs, we find that the heating effects dominate for stronger pump fields. Furthermore, the Hall response also contains a contribution arising from a population imbalance, which is difficult to discern from the contribution originating from the induced Berry curvature.

This is where TR-ARPES can provide valuable insights. The energy resolution allows us to observe the effective bands and their occupation even in a hot state. Moreover, measuring circular dichroism provides a direct link to the topological state. *Intrinsic* dichroism arises due to the orbital magnetization [49], which is proportional to the Berry curvature in the simple effective model. For graphene, in particular, the dichroism is a direct map of the induced pseudospin texture, which is intimately connected to the topological state. Combining accurate one-step calculations of the photoemission matrix elements with atomistic time-dependent simulations provides a state-of-the-art approach to TR-ARPES and the circular dichroism in particular. We show that the thus obtained band-resolved dichroism is in line with the pseudospin properties and is sizable even when the Floquet gap cannot be observed. Furthermore, the dichroism is robust against scattering effects and dissipation, which is corroborated by a steady-state model.

Measuring circular dichroism in ARPES—accompanied by a predictive theory—thus provides a tool for tracing topological properties in and out of equilibrium in an unprecedented way with full band (and even spatial [77,78]) resolution in real time. More generally, our proposal can be used to detect Berry curvature in nonequilibrium systems even in the absence of a clear Hall response. Examples are topological states in the excited-state manifold [20] or nonequilibrium tuning of the Berry curvature [21,79]. This new capability may boost the discovery and understanding of transient topological phenomena.

ACKNOWLEDGMENTS

APPENDIX A: TIGHT-BINDING HAMILTONIAN AND ORBITALS

We describe the electronic structure of graphene at the level of the next-nearest-neighbor TB model defined by

$$\hat{H}_0 = \sum_{\mathbf{k}} \sum_{j,j',\sigma} h_{jj'}(\mathbf{k}) \hat{c}^\dagger_{\mathbf{k}j\sigma} \hat{c}_{\mathbf{k}j'\sigma}. \tag{A1}$$

Here, $\hat{c}^\dagger_{\mathbf{k}j\sigma}$ ($\hat{c}_{\mathbf{k}j\sigma}$) creates (annihilates) an electron with momentum $\mathbf{k}$ and spin σ; j labels the sublattice site within the unit cell. Employing a compact matrix notation, the Hamiltonian is constructed in the TB approximation as

$$\mathbf{h}(\mathbf{k}) = \begin{pmatrix} 0 & g(\mathbf{k}) \\ g^*(\mathbf{k}) & 0 \end{pmatrix} \tag{A2}$$

with

$$g(\mathbf{k}) = -J e^{i\mathbf{k}\cdot\boldsymbol{\tau}} (1 + e^{-i\mathbf{k}\cdot\mathbf{a}_2} + e^{-i\mathbf{k}\cdot(\mathbf{a}_1+\mathbf{a}_2)}), \tag{A3}$$

where $\mathbf{a}_{1,2}$ denote the lattice vectors and $\boldsymbol{\tau} = \mathbf{t}_B - \mathbf{t}_A$ the vector connecting the sublattice sites. The hopping amplitude is chosen as $J = 2.628$ eV.

The Bloch states $\psi_{\mathbf{k}\alpha}(\mathbf{r})$ are obtained by the Wannier representation

$$\psi_{\mathbf{k}\alpha}(\mathbf{r}) = \frac{1}{\sqrt{N}} \sum_{\mathbf{R}} \sum_j C_{\alpha j}(\mathbf{k}) e^{i\mathbf{k}\cdot(\mathbf{R}+\mathbf{t}_j)} w_j(\mathbf{r} - \mathbf{R})$$

$$\equiv \sum_j C_{\alpha j}(\mathbf{k}) \phi_{\mathbf{k}j}(\mathbf{r}), \tag{A4}$$

where the coefficients $C_{\alpha j}(\mathbf{k})$ are the eigenvectors of the Hamiltonian (A2). The Wannier orbitals are approximated by Gaussian wave functions of the type

$$w_j(\mathbf{r}) = C_j z e^{-\alpha_j(\mathbf{r}-\mathbf{t}_j)^2}. \tag{A5}$$

The parameters C_j and α_j are fitted to atomic orbitals.

APPENDIX B: ONE-STEP CALCULATION OF MATRIX ELEMENTS

The photoemission intensity is governed by Fermi's golden rule given by

$$I(\mathbf{p}, \varepsilon_f) \propto |\langle \chi_{\mathbf{p},p_\perp} | \hat{\varepsilon} \cdot \hat{D} | \psi_{\mathbf{k}\alpha} \rangle|^2 \delta(\varepsilon_{\mathbf{k}\alpha} + \hbar\omega - \varepsilon_f). \tag{B1}$$

Here, the photon energy is given by $\hbar\omega$, and $\varepsilon_f = (p^2 + p_\perp^2)/2$ is the energy of the photoelectron final state $|\chi_{\mathbf{p},p_\perp}\rangle$. The matrix element of the dipole operator $\hat{D}$ and the polarization direction $\hat{\varepsilon}$ determine the selection rules. The in-plane momentum $\mathbf{p}$ is identical to the quasimomentum $\mathbf{k}$ up to a reciprocal lattice vector. While formally equivalent, the choice of the gauge for the transition operator $\hat{D}$ plays an important role in developing accurate approximations. In this work, we use the momentum operator $\hat{D} = \hat{\mathbf{p}} = (\hbar/i)\nabla$. However, for capturing effects such as circular dichroism, accurate final states $|\chi_{\mathbf{p},p_\perp}\rangle$ are required. For instance, approximating the final states by plane waves, the circular dichroism vanishes. Therefore, we compute $|\chi_{\mathbf{p},p_\perp}\rangle$ explicitly as eigenstates of a model potential. In particular, we construct a muffin-type scattering potential of the form

$$V(\mathbf{r}) = \sum_{\mathbf{R}} v_0(|\mathbf{r} - \mathbf{R}|), \tag{B2}$$

where the sum runs over all lattice sites. The spherical atom-centered potential is modeled by a smoothed boxlike dependence $v_0(r) = -V_0/\{1 + \exp[a_0(r - r_0)]\}$. The parameters V_0, a_0, and r_0 are adjusted to approximate the *ab initio* photoemission spectra (see below).

The final states are Bloch states with respect to the in-plane momentum, while they obey time-reversed LEED asymptotic boundary conditions in the out-of-plane (z) direction. Thus, it is convenient to expand the final states as

$$\chi_{\mathbf{p},p_\perp}(\mathbf{r}) = \sum_{\mathbf{G}} e^{i(\mathbf{p}+\mathbf{G})\cdot\mathbf{r}} \xi_{\mathbf{p},p_\perp;\mathbf{G}}(z). \tag{B3}$$

The photoelectron momentum $\mathbf{p}$ is identical to the crystal momentum $\mathbf{k} + \mathbf{G_0}$ of the initial Bloch states due to in-plane momentum conservation (up to a reciprocal lattice vector $\mathbf{G_0}$). Assuming photoemission from the first BZ ($\mathbf{G_0} = 0$), the expansion coefficients in Eq. (B3) are fixed by

$$\chi_{\mathbf{p},p_\perp}(\mathbf{r}) \to e^{i\mathbf{k}\cdot\mathbf{r}} + \sum_{\mathbf{G}} R_{\mathbf{G}} e^{-i(\mathbf{k}+\mathbf{G})\cdot\mathbf{r}}, \qquad (z \to \infty),$$

$$\chi_{\mathbf{p},p_\perp}(\mathbf{r}) \to \sum_{\mathbf{G}} T_{\mathbf{G}} e^{i(\mathbf{k}+\mathbf{G})\cdot\mathbf{r}}, \qquad (z \to -\infty), \tag{B4}$$

where $R_{\mathbf{G}}$ and $T_{\mathbf{G}}$ are reflection and transmission coefficients, respectively. Expanding the potential in plane waves,

$$V(\mathbf{r}) = \sum_{\mathbf{G}} e^{i\mathbf{G}\cdot\mathbf{r}} V_G(z), \tag{B5}$$

the final states (B3) are determined by the Schrödinger equation

$$\sum_{\mathbf{G}'} \left[\left(-\frac{\partial_z^2}{2} + \frac{(\mathbf{p}+\mathbf{G})^2}{2} \right) \delta_{\mathbf{G},\mathbf{G}'} + V_{\mathbf{G}-\mathbf{G}'}(z) \right] \xi_{\mathbf{p},p_\perp;\mathbf{G}'}(z)$$
$$= \left(\frac{\mathbf{p}^2}{2} + \frac{p_\perp^2}{2} \right) \xi_{\mathbf{p},p_\perp;\mathbf{G}}(z). \tag{B6}$$

We solve Eq. (B6) together with the boundary condition (B4) employing the renormalized Numerov method as in Ref. [80].

After obtaining the final states, the matrix elements $M_\alpha(\mathbf{k}, p_\perp) = \langle \chi_{\mathbf{k},p_\perp} | \hat{e} \cdot \hat{D} | \psi_{\mathbf{k}\alpha} \rangle$ are computed by

$$M_\alpha(\mathbf{k}, p_\perp) = \sum_{\mathbf{G}} \hat{e} \cdot (\mathbf{k}+\mathbf{G}) \int_{-\infty}^{\infty} dz \xi^*_{\mathbf{p},p_\perp;\mathbf{G}}(z) \phi_{\mathbf{k}\alpha;\mathbf{G}}(z), \tag{B7}$$

where $\phi_{\mathbf{k}\alpha;\mathbf{G}}(z)$ denote the plane-wave expansion coefficients of the Bloch states (A4).

The thus calculated matrix elements are benchmarked against *ab initio* calculations based on time-dependent density function theory (TDDFT) (analogous to Ref. [49]). We find the best agreement of the resulting ARPES spectra with the first-principles results for $V_0 = 3.0$, $a_0 = 5$, and $r_0 = 1$ (atomic units). As a characteristic benchmark, we compute the total intensity $I_{\text{tot}}(\mathbf{k}, \varepsilon_f)$ and the circular dichroism $I_{\text{CD}}(\mathbf{k}, \varepsilon_f)$ along the path shown in the inset in Fig. 8. As is known from theory [49] and experiment [43,44], this region in momentum space is where the circular dichroism is most pronounced (while it vanishes in the $\Gamma - K$ direction).

Figure 8 shows $I_{\text{tot}}(\mathbf{k}, \varepsilon_f)$ and $I_{\text{CD}}(\mathbf{k}, \varepsilon_f)$ within the TB+one-step theory and compares it to the first-principles calculations. Except for the exact magnitude of the circular dichroism, the TB+one-step approach matches the TDDFT results very well, thus endorsing it as an excellent method for the description of qualitative behavior (especially close to the Dirac point).

APPENDIX C: TIME-DEPENDENT NONEQUILIBRIUM GREEN'S FUNCTIONS CALCULATIONS

We treat the dynamics in pumped graphene including *e-e* scattering as well as *e*-ph coupling within the framework of the TD-NEGF approach based on the single-particle GF defined on the Kadanoff-Baym contour $\mathcal{C}$:
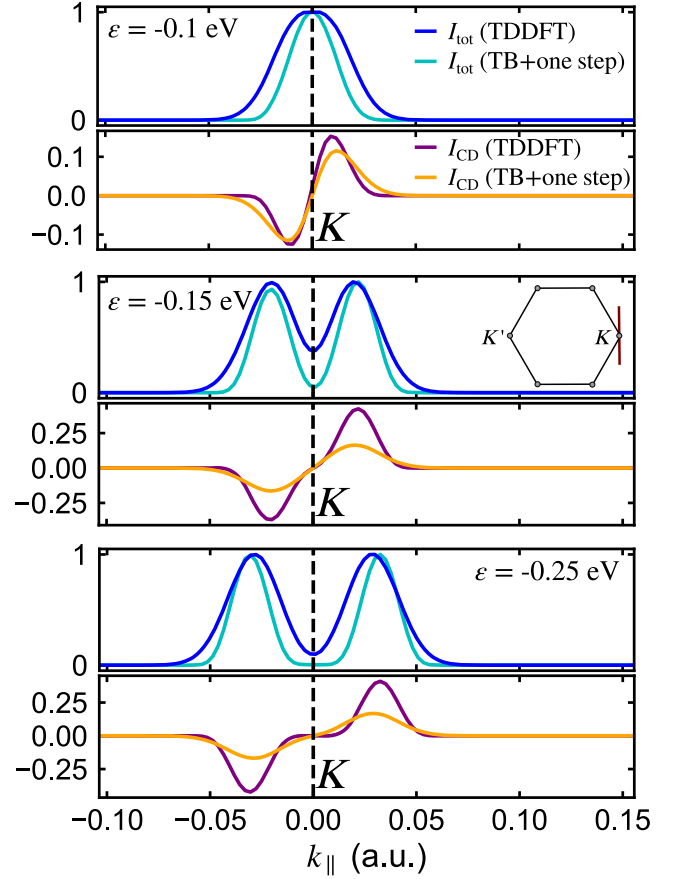

FIG. 8. Comparison of the ARPES intensity $I(\mathbf{k}, \varepsilon_f)$ for different binding energies within the *ab initio* method and the TB+one-step approach. We show the characteristic path in the BZ orthogonal to Γ-K passing through K (see inset).

$$G_{jj',\sigma}(\mathbf{k}; t, t') = -i\langle T_{\mathcal{C}} \hat{c}_{\mathbf{k}j\sigma}(t) \hat{c}^\dagger_{\mathbf{k}j'\sigma}(t') \rangle. \tag{C1}$$

Here, $T_{\mathcal{C}}$ denotes the contour ordering symbol. Since the spin-orbit coupling is negligibly small in graphene, we drop the spin index in what follows. The contour GF (C1) obeys the equation of motion

$$(i\partial_t - \mathbf{h}^{\text{MF}}(\mathbf{k}, t))\mathbf{G}(\mathbf{k}; t, t') = \delta_{\mathcal{C}}(t, t')$$
$$+ \int_{\mathcal{C}} d\bar{t} \mathbf{\Sigma}(\mathbf{k}; t, \bar{t})\mathbf{G}(\mathbf{k}; \bar{t}, t'). \tag{C2}$$

Here, we employ a compact matrix notation. The self-energy $\mathbf{\Sigma}(\mathbf{k}; t, t')$ captures all interaction effects beyond the mean-field (MF) Hamiltonian $\mathbf{h}^{\text{MF}}(\mathbf{k}, t)$. Projecting onto observable times using the Langreth rules transforms the equation of motion (C2) into the usual Kadanoff-Baym equations (KBEs). Solving the KBEs poses a considerable computational challenge, as the computational effort grows as N_t^3 with N_t time steps. To reduce the numerical effort and the memory demands, we employ the generalized

Kadanoff-Baym ansatz (GKBA). The GKBA transforms the two-time KBEs to the single-time kinetic equation for the single-particle density matrix $\rho(\mathbf{k}, t)$:

$$\partial_t \rho(\mathbf{k}, t) + i[\mathbf{h}^{\mathrm{MF}}(\mathbf{k}, t), \rho(\mathbf{k}, t)] = -[\mathbf{I}(\mathbf{k}, t) + \mathrm{H.c.}],$$
(C3)

where the collision integral $\mathbf{I}(\mathbf{k}, t)$ is defined by

$$\mathbf{I}(\mathbf{k}, t) = \int_{-\infty}^{t} d\bar{t} (\mathbf{\Sigma}^{<}(\mathbf{k}; t, \bar{t}) \mathbf{G}^{A}(\mathbf{k}; \bar{t}, t) + \mathbf{\Sigma}^{R}(\mathbf{k}; t, \bar{t}) \mathbf{G}^{<}(\mathbf{k}; \bar{t}, t)).$$
(C4)

Correlations of the initial state $\rho(\mathbf{k}; t = 0)$ are built in by adiabatic switching: At $t = -\infty$, the equilibrium density matrix is determined by the MF treatment, while correlation effects are gradually incorporated by replacing $\mathbf{\Sigma}(\mathbf{k}; t, t') \rightarrow f(t) f(t') \mathbf{\Sigma}(\mathbf{k}; t, t')$ with a smooth switch-on function $f(t)$. However, Eqs. (C3) and (C4) are not closed in terms of $\rho(\mathbf{k}, t)$ since, in principle, information on the whole two-time dependence of the GF enters the collision integral (C4). Within the GKBA, the two-time dependence, which captures spectral information, is approximated by

$$\mathbf{G}^{<}(\mathbf{k}; t, t') = -\mathbf{G}^{R}(\mathbf{k}; t, t') \rho(\mathbf{k}, t') + \rho(\mathbf{k}, t) \mathbf{G}^{A}(\mathbf{k}; t, t'),$$
(C5a)

$$\mathbf{G}^{>}(\mathbf{k}; t, t') = \mathbf{G}^{R}(\mathbf{k}; t, t') \bar{\rho}(\mathbf{k}, t') - \bar{\rho}(\mathbf{k}, t) \mathbf{G}^{A}(\mathbf{k}; t, t'),$$
(C5b)

where $\bar{\rho}(\mathbf{k}, t) = 1 - \rho(\mathbf{k}, t')$. Here we approximate $\mathbf{G}^{R}(\mathbf{k}; t, t')$ by the MF GF

$$(i\partial_t - \mathbf{h}^{\mathrm{MF}}(\mathbf{k}, t)) \mathbf{G}^{R}(\mathbf{k}; t, t') = \delta(t - t').$$
(C6)

1. Electron-electron interactions

As has been shown in Ref. [51], graphene can be treated to a good approximation as an effective Hubbard model with $U \approx 1.6|J|$, which we adopt in this work. Thus, we consider

$$\hat{H}_{e-e} = \frac{U}{2} \sum_{\mathbf{R}} \sum_{j,\sigma} \left(\hat{n}_{\mathbf{R}j\sigma} - \frac{1}{2} \right) \left(\hat{n}_{\mathbf{R}j\bar{\sigma}} - \frac{1}{2} \right),$$
(C7)

where $\hat{n}_{\mathbf{R}j\sigma}$ is the density operator for unit cell $\mathbf{R}$.

The value for U is clearly in the weakly interacting regime. Therefore, we employ the second-order expansion in the Coulomb interaction (second Born approximation) for the self-energy:

$$\Sigma_{jj'}^{e-e, \gtrless}(\mathbf{k}; t, t') = \frac{U^2}{N_k^2} \sum_{\mathbf{q}, \mathbf{p}} G_{jj'}^{\gtrless}(\mathbf{k} - \mathbf{q}; t, t') G_{jj'}^{\gtrless}(\mathbf{q} + \mathbf{p}; t, t') \times G_{j'j}^{\lessgtr}(\mathbf{p}; t', t).$$
(C8)

Here, N_k denotes the number of points sampling the BZ.

2. Electron-phonon coupling

We also include e-ph interactions, which are modeled by the Hamiltonian

$$\hat{H}_{e\text{-ph}} = \frac{1}{\sqrt{N_k}} \sum_{\mathbf{q}, \nu} \frac{1}{\sqrt{M_C \omega_{\mathbf{q}\nu}}} \sum_{\mathbf{k}} \sum_{jl, \sigma} \Gamma_{jl}^{\nu}(\mathbf{q}) \hat{c}_{\mathbf{k}-\mathbf{q}j\sigma}^{\dagger} \hat{c}_{\mathbf{k}l\sigma} \hat{X}_{\mathbf{q}\nu},$$
(C9)

where we include the phonon modes $\nu \in \{\mathrm{LA, TA, LO, TO}\}$. $\omega_{\mathbf{q}\nu}$ stands for their dispersion; M_C is the mass of the carbon atom. The phonon coordinate operator is defined by $\hat{X}_{\mathbf{q}\nu} = (\hat{b}_{\mathbf{q}\nu} + \hat{b}_{-\mathbf{q}\nu}^{\dagger})/\sqrt{2}$.

Systematic studies and transport experiments [52,81] have demonstrated the feasibility of a weak-coupling treatment. Hence, we employ the (non-self-consistent) Midgal approximation. The e-ph contribution to the self-energy is then given by

$$\Sigma_{jj'}^{e\text{-ph}, \gtrless}(\mathbf{k}; t, t') = \frac{i}{N_k} \sum_{\mathbf{q}, \nu} \frac{1}{M_C \omega_{\mathbf{q}\nu}} \sum_{ll'} \Gamma_{jl}^{\nu}(\mathbf{q}) G_{ll'}^{\gtrless}(\mathbf{k} - \mathbf{q}; t, t') \times \Gamma_{l'j'}^{\nu}(\mathbf{q}) D_{\nu}^{\gtrless}(\mathbf{q}; t, t').$$
(C10)

Here, $D_{\nu}^{\gtrless}(\mathbf{q}; t, t')$ denotes the free phonon GF.

The e-ph coupling matrix elements $\Gamma_{jl}^{\nu}(\mathbf{q})$ are computed from the symmetry of the phonon modes and the Bloch states. In this work, we adopt the canonical modes from Ref. [82], while the e-ph couplings are taken from the TB model from Ref. [52]. For completeness, we gather the formulas for the couplings below:

$$\mathbf{\Gamma}^{\mathrm{TA}}(\mathbf{q}) = |\mathbf{q}| \begin{pmatrix} 2\alpha & \beta_A \mathbf{e}_{-}(\mathbf{q})^2 \\ \beta_A \mathbf{e}_{+}(\mathbf{q})^2 & 2\alpha \end{pmatrix},$$
(C11a)

$$\mathbf{\Gamma}^{\mathrm{LA}}(\mathbf{q}) = |\mathbf{q}| \begin{pmatrix} 0 & \beta_A \mathbf{e}_{-}(\mathbf{q})^2 \\ \beta_A \mathbf{e}_{+}(\mathbf{q})^2 & 0 \end{pmatrix},$$
(C11b)

$$\mathbf{\Gamma}^{\mathrm{LO}}(\mathbf{q}) = i \begin{pmatrix} 0 & \beta_O \mathbf{e}_{+}(\mathbf{q}) \\ -\beta_O \mathbf{e}_{-}(\mathbf{q}) & 0 \end{pmatrix},$$
(C11c)

$$\mathbf{\Gamma}^{\mathrm{TO}}(\mathbf{q}) = \begin{pmatrix} 0 & -\beta_O \mathbf{e}_{+}(\mathbf{q}) \\ -\beta_O \mathbf{e}_{-}(\mathbf{q}) & 0 \end{pmatrix}.$$
(C11d)

Here, $\mathbf{e}_{\pm}(\mathbf{q}) = (q_x \pm iq_y)/|\mathbf{q}|$. For the constants α, β_A, and β_O we adopt the GW values from Ref. [52].

3. Spectral corrections

The GKBA underestimates self-energy effects for the two-time dependence of the GF. Therefore, we correct the retarded GF by the static correlation correction from Ref. [60] by solving

$$(i\partial_t - \mathbf{h}^{\mathrm{MF}}(\mathbf{k}, t) - \tilde{\mathbf{\Sigma}}(\mathbf{k}, t))\tilde{\mathbf{G}}^R(\mathbf{k}; t, t') = \delta(t - t'). \quad (C12)$$

Here, the effective one-time self-energy is approximated by

$$\tilde{\mathbf{\Sigma}}(\mathbf{k}, t) = \int d\bar{t}\mathbf{\Sigma}^R(\mathbf{k}, t, t - \bar{t}). \quad (C13)$$

Tests show that these corrections have little influence on the dynamics of $\rho(\mathbf{k}, t)$. Therefore, we employ the correction in a "one-shot" fashion: After obtaining $\rho(\mathbf{k}, t)$ for all time steps, we construct the lesser and greater GFs according to Eq. (C5), substitute them into Eq. (C13), and compute the retarded GF from Eq. (C12). Finally, the corrected lesser GF is obtained from Eq. (C5), replacing $\mathbf{G}^R \to \tilde{\mathbf{G}}^R$.

4. Numerical details

The GKBA calculations are performed with a highly accurate, in-house compute code. All collision integrals (C4) are computed using fifth-order Gregory quadrature [83], while the equation of motion (C3) is solved with a fifth-order Adams-Moulton predictor-corrector scheme. We use $N_t = 4500$ to $N_t = 5600$ equidistant time points and a time step of $h = 0.5$ a.u. (convergence is checked). The full first BZ is sampled by an $N_k = 96 \times 96$ grid in momentum space.

APPENDIX D: FLOQUET STEADY-STATE FORMALISM

The Floquet NESS formalism is a powerful tool for describing the dynamically equilibrated balance of absorption, scattering, and dissipation [75]. Here we consider the noninteracting graphene system, where each lattice site is coupled to a fermionic bath characterized by an embedding self-energy [55]. To determine the steady state, one first solves for the retarded Floquet GF

$$[\hat{\mathcal{G}}^R(\mathbf{k}, \omega)]^{-1} = \omega - \hat{\mathcal{H}}(\mathbf{k}) - \hat{\Sigma}^R(\omega), \quad (D1)$$

where $\hat{\mathcal{H}}(\mathbf{k})$ denotes the matrix representation of the Floquet Hamiltonian (4) in the combined space of orbitals and Floquet indices. For the retarded self-energy, we invoke the wideband limit approximation $\Sigma^R_{nj,n'j'}(\omega) = -i\delta_{nn'}\delta_{jj'}\gamma/2$. The parameter γ describes the coupling strength. The lesser component of the self-energy representing the occupation of the bath is given by

$$\Sigma^<_{nj,n'j'}(\omega) = i\delta_{nn'}\delta_{jj'}\gamma f(\omega - \mu + n\omega_p), \quad (D2)$$

where $f(\omega)$ denotes the Fermi distribution with inverse temperature $\beta = 1/T_{\mathrm{eff}}$; μ is the chemical potential of the reservoir, which is assumed to be aligned with the chemical potential of undoped graphene. The lesser Floquet GF is then determined by the Keldysh equation

$$\hat{\mathcal{G}}^<(\mathbf{k}, \omega) = \hat{\mathcal{G}}^R(\mathbf{k}, \omega)\hat{\Sigma}^<(\omega)[\hat{\mathcal{G}}^R(\mathbf{k}, \omega)]^\dagger. \quad (D3)$$

Finally, the physical GF is obtained by switching to the two-time representation

$$G^<_{jj'}(\mathbf{k}; t, t') = \sum_{nn'} \int_{-\omega_p/2}^{\omega_p/2} \frac{d\omega}{2\pi} \mathcal{G}^<_{nj,n'j'}(\mathbf{k}; \omega) \times e^{-i\omega(t-t')}e^{-in\omega_p t}e^{in'\omega_p t'}. \quad (D4)$$

The thus obtained GF is substituted into Eq. (10), which yields the steady-state photoemission expression (13).

The Hall response is calculated (ignoring vertex corrections) as in Ref. [14]:

$$\sigma_{xy}(\omega) = \frac{1}{\omega}\frac{2}{N_k S_c}\mathrm{ReTr}\sum_{\mathbf{k}} \int_{-\omega_p/2}^{\omega_p/2} \frac{d\omega'}{2\pi}(\hat{v}_x(\mathbf{k})\hat{\mathcal{G}}^R(\mathbf{k}, \omega' + \omega)\hat{v}_y(\mathbf{k})\hat{\mathcal{G}}^<(\mathbf{k}, \omega') + \hat{v}_x(\mathbf{k})\hat{\mathcal{G}}^<(\mathbf{k}, \omega' + \omega)\hat{v}_y(\mathbf{k})\hat{\mathcal{G}}^A(\mathbf{k}, \omega'))$$

$$(D5)$$

in the limit $\omega \to 0$. Here, the velocity matrix elements in the Floquet representation are defined by

$$v_{\alpha,nj,n'j'}(\mathbf{k}) = \frac{1}{T_p}\int_0^{T_p} dt \frac{\partial}{\partial k_\alpha} h_{jj'}(\mathbf{k} - \mathbf{A}_p(t))e^{i(n-n')\omega_p t}. \quad (D6)$$

At a given coupling strength γ (and fixed pump parameters), the only adjustable parameter is the effective temperature T_{eff}, which can be different from the electronic temperature T_{el}. To obtain T_{eff} corresponding to a certain T_{el}, we compute the averaged kinetic energy (without a pulse) by

$$E_{\mathrm{kin}} = \frac{1}{N_k}\sum_{\mathbf{k}}\sum_{jj'} h_{jj'}(\mathbf{k})\frac{1}{T_p}\int_0^{T_p} dt\, G^<_{jj'}(\mathbf{k}, t, t) \quad (D7)$$

from the physical GF (D4) as a function of T_{eff}. Comparing to the dependence $E_{\mathrm{kin}}(T_{\mathrm{el}})$ in thermal equilibrium then allows us to determine the relation between T_{eff} and T_{el}.

[1] M. Z. Hasan and C. L. Kane, *Colloquium: Topological Insulators*, Rev. Mod. Phys. **82,** 3045 (2010).

[2] X.-L. Qi, T. L. Hughes, and S.-C. Zhang, *Topological Field Theory of Time-Reversal Invariant Insulators*, Phys. Rev. B **78,** 195424 (2008).

[3] L. Kou, Y. Ma, Z. Sun, T. Heine, and C. Chen, *Two-Dimensional Topological Insulators: Progress and Prospects*, J. Phys. Chem. Lett. **8,** 1905 (2017).

[4] A. Marrazzo, M. Gibertini, D. Campi, N. Mounet, and N. Marzari, *Prediction of a Large-Gap and Switchable Kane-Mele Quantum Spin Hall Insulator*, Phys. Rev. Lett. **120,** 117701 (2018).

[5] S. Tang *et al.*, *Quantum Spin Hall State in Monolayer 1T'-*WTe$_2$, Nat. Phys. **13,** 683 (2017).

[6] L. Muechler, A. Alexandradinata, T. Neupert, and R. Car, *Topological Nonsymmorphic Metals from Band Inversion*, Phys. Rev. X **6,** 041069 (2016).

[7] C. L. Kane and E. J. Mele, *Quantum Spin Hall Effect in Graphene*, Phys. Rev. Lett. **95,** 226801 (2005).

[8] C. L. Kane and E. J. Mele, z_2 *Topological Order and the Quantum Spin Hall Effect*, Phys. Rev. Lett. **95,** 146802 (2005).

[9] C. Weeks, J. Hu, J. Alicea, M. Franz, and R. Wu, *Engineering a Robust Quantum Spin Hall State in Graphene via Adatom Deposition*, Phys. Rev. X **1,** 021001 (2011).

[10] A. H. C. Neto and F. Guinea, *Impurity-Induced Spin-Orbit Coupling in Graphene*, Phys. Rev. Lett. **103,** 026804 (2009).

[11] S. Abdelouahed, A. Ernst, J. Henk, I. V. Maznichenko, and I. Mertig, *Spin-Split Electronic States in Graphene: Effects due to Lattice Deformation, Rashba Effect, and Adatoms by First Principles*, Phys. Rev. B **82,** 125424 (2010).

[12] T. Oka and H. Aoki, *Photovoltaic Hall Effect in Graphene*, Phys. Rev. B **79,** 081406(R) (2009).

[13] N. H. Lindner, G. Refael, and V. Galitski, *Floquet Topological Insulator in Semiconductor Quantum Wells*, Nat. Phys. **7,** 490 (2011).

[14] T. Mikami, S. Kitamura, K. Yasuda, N. Tsuji, T. Oka, and H. Aoki, *Brillouin-Wigner Theory for High-Frequency Expansion in Periodically Driven Systems: Application to Floquet Topological Insulators*, Phys. Rev. B **93,** 144307 (2016).

[15] H. Dehghani, T. Oka, and A. Mitra, *Out-of-Equilibrium Electrons and the Hall Conductance of a Floquet Topological Insulator*, Phys. Rev. B **91,** 155422 (2015).

[16] H. Dehghani and A. Mitra, *Optical Hall Conductivity of a Floquet Topological Insulator*, Phys. Rev. B **92,** 165111 (2015).

[17] G. Jotzu, M. Messer, R. Desbuquois, M. Lebrat, T. Uehlinger, D. Greif, and T. Esslinger, *Experimental Realization of the Topological Haldane Model with Ultracold Fermions*, Nature (London) **515,** 237 (2014).

[18] L. D'Alessio and M. Rigol, *Dynamical Preparation of Floquet Chern Insulators*, Nat. Commun. **6,** 8336 (2015).

[19] H. Hübener, U. De Giovannini, and A. Rubio, *Phonon Driven Floquet Matter*, Nano Lett. **18,** 1535 (2018).

[20] M. Claassen, C. Jia, B. Moritz, and T. P. Devereaux, *All-Optical Materials Design of Chiral Edge Modes in Transition-Metal Dichalcogenides*, Nat. Commun. **7,** 13074 (2016).

[21] H. Hübener, M. A. Sentef, U. De Giovannini, A. F. Kemper, and A. Rubio, *Creating Stable Floquet-Weyl Semimetals by Laser-Driving of 3D Dirac Materials*, Nat. Commun. **8,** 13940 (2017).

[22] U. De Giovannini, H. Hübener, and A. Rubio, *Monitoring Electron-Photon Dressing in* WSe$_2$, Nano Lett. **16,** 7993 (2016).

[23] Y. H. Wang, H. Steinberg, P. Jarillo-Herrero, and N. Gedik, *Observation of Floquet-Bloch States on the Surface of a Topological Insulator*, Science **342,** 453 (2013).

[24] F. Mahmood, C.-K. Chan, Z. Alpichshev, D. Gardner, Y. Lee, P. A. Lee, and N. Gedik, *Selective Scattering between Floquet-Bloch and Volkov States in a Topological Insulator*, Nat. Phys. **12,** 306 (2016).

[25] M. Reutzel, A. Li, and H. Petek, *Coherent Two-Dimensional Multiphoton Photoelectron Spectroscopy of Metal Surfaces*, Phys. Rev. X **9,** 011044 (2019).

[26] Q. T. Vu, H. Haug, O. D. Mücke, T. Tritschler, M. Wegener, G. Khitrova, and H. M. Gibbs, *Light-Induced Gaps in Semiconductor Band-to-Band Transitions*, Phys. Rev. Lett. **92,** 217403 (2004).

[27] J. W. McIver, B. Schulte, F.-U. Stein, T. Matsuyama, G. Jotzu, G. Meier, and A. Cavalleri, *Light-Induced Anomalous Hall Effect in Graphene*, Nat. Phys. **16,** 38 (2020).

[28] S. A. Sato, J. W. McIver, M. Nuske, P. Tang, G. Jotzu, B. Schulte, H. Hübener, U. De Giovannini, L. Mathey, M. A. Sentef, A. Cavalleri, and A. Rubio, *Microscopic Theory for the Light-Induced Anomalous Hall Effect in Graphene*, Phys. Rev. B **99,** 214302 (2019).

[29] S. A. Sato, P. Tang, M. A. Sentef, U. De Giovannini, H. Hübener, and A. Rubio, *Light-Induced Anomalous Hall Effect in Massless Dirac Fermion Systems and Topological Insulators with Dissipation*, New J. Phys. **21,** 093005 (2019).

[30] E. Kandelaki and M. S. Rudner, *Many-Body Dynamics and Gap Opening in Interacting Periodically Driven Systems*, Phys. Rev. Lett. **121,** 036801 (2018).

[31] S. A. Sato, U. De Giovannini, S. Aeschlimann, I. Gierz, H. Hübener, and A. Rubio, *Floquet States in Dissipative Open Quantum Systems*, arXiv:1912.03176.

[32] I. Gierz, F. Calegari, S. Aeschlimann, M. C. Cervantes, C. Cacho, R. T. Chapman, E. Springate, S. Link, U. Starke, C. R. Ast, and A. Cavalleri, *Tracking Primary Thermalization Events in Graphene with Photoemission at Extreme Time Scales*, Phys. Rev. Lett. **115,** 086803 (2015).

[33] I. Gierz and A. Cavalleri, *Electronic-Structural Dynamics in Graphene*, Struct. Dyn. **3,** 051301 (2016).

[34] M. X. Na, A. K. Mills, F. Boschini, M. Michiardi, B. Nosarzewski, R. P. Day, E. Razzoli, A. Sheyerman, M. Schneider, G. Levy, S. Zhdanovich, T. P. Devereaux, A. F. Kemper, D. J. Jones, and A. Damascelli, *Direct Determination of Mode-Projected Electron-Phonon Coupling in the Time Domain*, Science **366,** 1231 (2019).

[35] F. Caruso, D. Novko, and C. Draxl, *Photoemission Signatures of Nonequilibrium Carrier Dynamics from First Principles*, Phys. Rev. B **101,** 035128 (2020).

[36] P. B. Allen, *Theory of Thermal Relaxation of Electrons in Metals*, Phys. Rev. Lett. **59**, 1460 (1987).

[37] H. Haug and S. W. Koch, *Quantum Theory of the Optical and Electronic Properties of Semiconductors* (World Scientific, Singapore, 1990).

[38] C. Gadermaier, A. S. Alexandrov, V. V. Kabanov, P. Kusar, T. Mertelj, X. Yao, C. Manzoni, D. Brida, G. Cerullo, and D. Mihailovic, *Electron-Phonon Coupling in High-Temperature Cuprate Superconductors Determined from Electron Relaxation Rates*, Phys. Rev. Lett. **105**, 257001 (2010).

[39] M. Sentef, A. F. Kemper, B. Moritz, J. K. Freericks, Z.-X. Shen, and T. P. Devereaux, *Examining Electron-Boson Coupling Using Time-Resolved Spectroscopy*, Phys. Rev. X **3**, 041033 (2013).

[40] S.-L. Yang, J. A. Sobota, D. Leuenberger, Y. He, M. Hashimoto, D. H. Lu, H. Eisaki, P. S. Kirchmann, and Z.-X. Shen, *Inequivalence of Single-Particle and Population Lifetimes in a Cuprate Superconductor*, Phys. Rev. Lett. **114**, 247001 (2015).

[41] J. D. Rameau, S. Freutel, A. F. Kemper, M. A. Sentef, J. K. Freericks, I. Avigo, M. Ligges, L. Rettig, Y. Yoshida, H. Eisaki, J. Schneeloch, R. D. Zhong, Z. J. Xu, G. D. Gu, P. D. Johnson, and U. Bovensiepen, *Energy Dissipation from a Correlated System Driven Out of Equilibrium*, Nat. Commun. **7**, 13761 (2016).

[42] V. V. Kabanov, *Electron-Electron and Electron-Phonon Relaxation in Metals Excited by Optical Pulse*, arXiv:2002.04343.

[43] Y. Liu, G. Bian, T. Miller, and T.-C. Chiang, *Visualizing Electronic Chirality and Berry Phases in Graphene Systems Using Photoemission with Circularly Polarized Light*, Phys. Rev. Lett. **107**, 166803 (2011).

[44] I. Gierz, M. Lindroos, H. Höchst, C. R. Ast, and K. Kern, *Graphene Sublattice Symmetry and Isospin Determined by Circular Dichroism in Angle-Resolved Photoemission Spectroscopy*, Nano Lett. **12**, 3900 (2012).

[45] Y. Wang and N. Gedik, *Circular Dichroism in Angle-Resolved Photoemission Spectroscopy of Topological Insulators*, Phys. Status Solidi RRL **7**, 64 (2013).

[46] S. R. Park, J. Han, C. Kim, Y. Y. Koh, C. Kim, H. Lee, H. J. Choi, J. H. Han, K. D. Lee, N. J. Hur, M. Arita, K. Shimada, H. Namatame, and M. Taniguchi, *Chiral Orbital-Angular Momentum in the Surface States of* Bi_2Se_3, Phys. Rev. Lett. **108**, 046805 (2012).

[47] E. Razzoli, T. Jaouen, M.-L. Mottas, B. Hildebrand, G. Monney, A. Pisoni, S. Muff, M. Fanciulli, N. C. Plumb, V. A. Rogalev, V. N. Strocov, J. Mesot, M. Shi, J. H. Dil, H. Beck, and P. Aebi, *Selective Probing of Hidden Spin-Polarized States in Inversion-Symmetric Bulk* MoS_2, Phys. Rev. Lett. **118**, 086402 (2017).

[48] S. Cho, J.-H. Park, J. Hong, J. Jung, B. S. Kim, G. Han, W. Kyung, Y. Kim, S.-K. Mo, J. D. Denlinger, J. H. Shim, J. H. Han, C. Kim, and S. R. Park, *Experimental Observation of Hidden Berry Curvature in Inversion-Symmetric Bulk* $2H$-WSe_2, Phys. Rev. Lett. **121**, 186401 (2018).

[49] M. Schüler, U. De Giovannini, H. Hübener, A. Rubio, M. A. Sentef, and P. Werner, *Local Berry Curvature Signatures in Dichroic Angle-Resolved Photoelectron Spec-*

[50] K. Volckaert *et al.*, *Momentum-Resolved Linear Dichroism in Bilayer* MoS_2, Phys. Rev. B **100**, 241406(R) (2019).

[51] M. Schüler, M. Rösner, T. O. Wehling, A. I. Lichtenstein, and M. I. Katsnelson, *Optimal Hubbard Models for Materials with Nonlocal Coulomb Interactions: Graphene, Silicene, and Benzene*, Phys. Rev. Lett. **111**, 036601 (2013).

[52] T. Sohier, M. Calandra, C.-H. Park, N. Bonini, N. Marzari, and F. Mauri, *Phonon-Limited Resistivity of Graphene by First-Principles Calculations: Electron-Phonon Interactions, Strain-Induced Gauge Field, and Boltzmann Equation*, Phys. Rev. B **90**, 125414 (2014).

[53] T. Sohier, M. Calandra, and F. Mauri, *Density-Functional Calculation of Static Screening in Two-Dimensional Materials: The Long-Wavelength Dielectric Function of Graphene*, Phys. Rev. B **91**, 165428 (2015).

[54] L. Pietronero, S. Strässler, H. R. Zeller, and M. J. Rice, *Electrical Conductivity of a Graphite Layer*, Phys. Rev. B **22**, 904 (1980).

[55] G. Stefanucci and R. van Leeuwen, *Nonequilibrium Many-Body Theory of Quantum Systems: A Modern Introduction* (Cambridge University Press, Cambridge, England, 2013).

[56] P. Lipavsky, V. Spicka, and B. Velicky, *Generalized Kadanoff-Baym Ansatz for Deriving Quantum Transport-Equations*, Phys. Rev. B **34**, 6933 (1986).

[57] N. Schlünzen, J.-P. Joost, F. Heidrich-Meisner, and M. Bonitz, *Nonequilibrium Dynamics in the One-Dimensional Fermi-Hubbard Model: Comparison of the Nonequilibrium Green-Functions Approach and the Density Matrix Renormalization Group Method*, Phys. Rev. B **95**, 165139 (2017).

[58] M. Schüler, J. C. Budich, and P. Werner, *Quench Dynamics and Hall Response of Interacting Chern Insulators*, Phys. Rev. B **100**, 041101(R) (2019).

[59] Y. Murakami, M. Schüler, S. Takayoshi, and P. Werner, *Ultrafast Nonequilibrium Evolution of Excitonic Modes in Semiconductors*, Phys. Rev. B **101**, 035203 (2020).

[60] S. Latini, E. Perfetto, A.-M. Uimonen, R. van Leeuwen, and G. Stefanucci, *Charge Dynamics in Molecular Junctions: Nonequilibrium Green's Function Approach Made Fast*, Phys. Rev. B **89**, 075306 (2014).

[61] J. K. Freericks, H. R. Krishnamurthy, and T. Pruschke, *Theoretical Description of Time-Resolved Photoemission Spectroscopy: Application to Pump-Probe Experiments*, Phys. Rev. Lett. **102**, 136401 (2009).

[62] W. Schattke and M. A. Van Hove, *Solid-State Photoemission and Related Methods: Theory and Experiment* (John Wiley & Sons, New York, 2008).

[63] A. Scrinzi, *t-SURFF: Fully Differential Two-Electron Photo-Emission Spectra*, New J. Phys. **14**, 085008 (2012).

[64] U. De Giovannini, H. Hübener, and A. Rubio, *A First-Principles Time-Dependent Density Functional Theory Framework for Spin and Time-Resolved Angular-Resolved Photoelectron Spectroscopy in Periodic Systems*, J. Chem. Theory Comput. **13**, 265 (2017).

[65] L. Miaja-Avila, C. Lei, M. Aeschlimann, J. L. Gland, M. M. Murnane, H. C. Kapteyn, and G. Saathoff, *Laser-Assisted Photoelectric Effect from Surfaces*, Phys. Rev. Lett. **97**, 113604 (2006).

troscopy from Two-Dimensional Materials, Sci. Adv. **6**, eaay2730 (2020).

[66] T. Kitagawa, T. Oka, A. Brataas, L. Fu, and E. Demler, *Transport Properties of Nonequilibrium Systems under the Application of Light: Photoinduced Quantum Hall Insulators without Landau Levels*, Phys. Rev. B **84**, 235108 (2011).

[67] I. Souza and D. Vanderbilt, *Dichroic f-Sum Rule and the Orbital Magnetization of Crystals*, Phys. Rev. B **77**, 054438 (2008).

[68] D. Xiao, M.-C. Chang, and Q. Niu, *Berry Phase Effects on Electronic Properties*, Rev. Mod. Phys. **82**, 1959 (2010).

[69] M. A. Sentef, M. Claassen, A. F. Kemper, B. Moritz, T. Oka, J. K. Freericks, and T. P. Devereaux, *Theory of Floquet Band Formation and Local Pseudospin Textures in Pump-Probe Photoemission of Graphene*, Nat. Commun. **6**, 7047 (2015).

[70] T. Cao, M. Wu, and S. G. Louie, *Unifying Optical Selection Rules for Excitons in Two Dimensions: Band Topology and Winding Numbers*, Phys. Rev. Lett. **120**, 087402 (2018).

[71] I. Gierz, J. Henk, H. Höchst, C. R. Ast, and K. Kern, *Illuminating the Dark Corridor in Graphene: Polarization Dependence of Angle-Resolved Photoemission Spectroscopy on Graphene*, Phys. Rev. B **83**, 121408(R) (2011).

[72] F. Peronaci, M. Schiró, and O. Parcollet, *Resonant Thermalization of Periodically Driven Strongly Correlated Electrons*, Phys. Rev. Lett. **120**, 197601 (2018).

[73] Y. Murakami, N. Tsuji, M. Eckstein, and P. Werner, *Nonequilibrium Steady States and Transient Dynamics of Conventional Superconductors under Phonon Driving*, Phys. Rev. B **96**, 045125 (2017).

[74] M. Schüler and P. Werner, *Tracing the Nonequilibrium Topological State of Chern Insulators*, Phys. Rev. B **96**, 155122 (2017).

[75] H. Aoki, N. Tsuji, M. Eckstein, M. Kollar, T. Oka, and P. Werner, *Nonequilibrium Dynamical Mean-Field Theory and Its Applications*, Rev. Mod. Phys. **86**, 779 (2014).

[76] This also holds when including e-e interactions only.

[77] E. L. Wong, A. J. Winchester, V. Pareek, J. Madéo, M. K. L. Man, and K. M. Dani, *Pulling Apart Photoexcited Electrons by Photoinducing an In-Plane Surface Electric Field*, Sci. Adv. **4**, eaat9722 (2018).

[78] I. Cucchi, I. Gutiérrez-Lezama, E. Cappelli, S. M. Walker, F. Y. Bruno, G. Tenasini, L. Wang, N. Ubrig, C. Barreteau, E. Giannini, M. Gibertini, A. Tamai, A. F. Morpurgo, and F. Baumberger, *Microfocus Laser-Angle-Resolved Photoemission on Encapsulated Mono-, Bi-, and Few-Layer 1T'-WTe$_2$*, Nano Lett. **19**, 554 (2019).

[79] E. J. Sie, J. W. McIver, Y.-H. Lee, L. Fu, J. Kong, and N. Gedik, *Valley-Selective Optical Stark Effect in monolayer WS$_2$*, Nat. Mater. **14**, 290 (2015).

[80] M. Schüler, Y. Pavlyukh, and J. Berakdar, *Nuclear-Wave-Packet Dynamics Mapped Out by Two-Center Interference in the HeH$_2^+$ Molecule*, Phys. Rev. A **89**, 063421 (2014).

[81] C.-H. Park, N. Bonini, T. Sohier, G. Samsonidze, B. Kozinsky, M. Calandra, F. Mauri, and N. Marzari, *Electron-Phonon Interactions and the Intrinsic Electrical Resistivity of Graphene*, Nano Lett. **14**, 1113 (2014).

[82] S. Piscanec, M. Lazzeri, F. Mauri, A. C. Ferrari, and J. Robertson, *Kohn Anomalies and Electron-Phonon Interactions in Graphite*, Phys. Rev. Lett. **93**, 185503 (2004).

[83] M. Schüler, D. Golež, Y. Murakami, N. Bittner, A. Hermann, H. U. R. Strand, P. Werner, and M. Eckstein, *NESSi: The Non-Equilibrium Systems Simulation Package*, Comput. Phys. Commun. **257**, 107484 (2020).